Available online at www.sciencedirect.com

SCIENCE DIRECT®

Biochimica et Biophysica Acta 1657 (2004) 82–104

BIOCHIMICA ET BIOPHYSICA ACTA
BBA

www.bba-direct.com

Review

Global and target analysis of time-resolved spectra☆

Ivo H.M. van Stokkum*, Delmar S. Larsen, Rienk van Grondelle

Department of Physics and Astronomy, Faculty of Sciences, Vrije Universiteit, De Boelelaan 1081, 1081 HV Amsterdam, The Netherlands

Received 29 December 2003; received in revised form 29 April 2004; accepted 29 April 2004

Abstract

In biological/bioenergetics research the response of a complex system to an externally applied perturbation is often studied. Spectroscopic measurements at multiple wavelengths are used to monitor the kinetics. These time-resolved spectra are considered as an example of multiway data. In this paper, the methodology for global and target analysis of time-resolved spectra is reviewed. To fully extract the information from the overwhelming amount of data, a model-based analysis is mandatory. This analysis is based upon assumptions regarding the measurement process and upon a physicochemical model for the complex system. This model is composed of building blocks representing scientific knowledge and assumptions. Building blocks are the instrument response function (IRF), the components of the system connected in a kinetic scheme, and anisotropy properties of the components. The combination of a model for the kinetics and for the spectra of the components results in a more powerful spectrotemporal model. The model parameters, like rate constants and spectra, can be estimated from the data, thus providing a concise description of the complex system dynamics. This spectrotemporal modeling approach is illustrated with an elaborate case study of the ultrafast dynamics of the photoactive yellow protein.

Keywords: Global analysis; Multiway data; Photoactive yellow protein; Spectrotemporal model; Target analysis; Time-resolved spectroscopy

Contents

Abbreviations: BR, bacteriorhodopsin; DADS, Decay Associated Difference Spectra; DAS, Decay Associated Spectra; EADS, Evolution Associated Difference Spectra; ESA, Excited State Absorption; ESI, Excited State Intermediate; GSA, Ground State Absorption; GSB, Ground State Bleach; GSI, Ground State Intermediate; I_0, first photocycle intermediate of PYP; I_1, second photocycle intermediate of PYP; IRF, instrument response function; MA, magic angle; mOD, milli optical density; NLLS, nonlinear least squares; pCA, *p*-coumaric acid; PYP, photoactive yellow protein; SADS, Species Associated Difference Spectra; SAS, Species Associated Spectra; SE, Stimulated Emission; SVD, Singular Value Decomposition

☆ Dedicated to Hans Spoelder, † 1.4.2003, who pioneered this field.

* Corresponding author. Tel.: +31-20-4447868; fax: +31-20-4447899.
E-mail address: ivo@nat.vu.nl (I.H.M. van Stokkum).

0005-2728/$ - see front matter © 2004 Elsevier B.V. All rights reserved.
doi:10.1016/j.bbabio.2004.04.011

1. Introduction

Time-resolved spectroscopy is a widely used tool in photophysics, photochemistry and photobiology to investigate the dynamic properties of complex systems [1,2]. Examples of such systems are chromophore–protein complexes essential for photosynthesis and photodetection, which are important model systems in bioenergetics. Many chromophoreprotein complexes traverse a photocycle, e.g. the proton pump bacteriorhodopsin (BR) [3,4] and the photodetector photoactive yellow protein (PYP) [5,6]. A key question in these chromophore–protein complexes is how the chromophore dynamics are modified by the protein [7,8]. This question can be adressed by time-resolved spectroscopy in combination with global and target analysis. Here global refers to a simultaneous analysis of all measurements, whereas target refers to the applicability of a particular target model. Phenomena occurring on a variety of time scales ranging from femtoseconds to seconds can be studied. The input to the system usually consists of a short pulse of high energy which is absorbed and triggers a series of reactions. These reactions are often accompanied by changes in the UV, visible or IR spectroscopic properties of the system which can be measured. The output of the system is thus a collection of measurements of a spectroscopic property, like absorption or emission, as a function of time and wavelength, which is called a time-resolved spectrum.

A time-resolved spectrum is the most well-known example of two-way data. These data are a collection of measurements in two dimensions (ways). The first dimension is the independent experimental spectral variable: wavelength λ or wave number $\bar{\nu}$, or magnetic field strength B, etc. The second dimension is an independent experimental variable to monitor spectral change: time t after excitation, temperature T, polarization dependence, acidity pH or pD, excitation wavelength, or quencher concentration [Q]. Adding a third dimension results in three-way data, of which the combination of time and wavelength with temperature or with quencher concentration are the most well known. In this paper we concentrate on time-resolved spectra, however, many of the methods are also applicable for other types of multiway data [9,10].

To unravel the processes underlying the observable spectroscopic changes, which result in overwhelming amounts of data, a model-based analysis of the measurements is mandatory. From an analysis perspective two problems can be distinguished: (a) when a parameterized model of the observations is available, the parameters have to be estimated in a statistically sound way; (b) when only a class of models is known, in addition also the ‘‘best’’ model needs to be determined.

Previously several methodological reviews have been written on global and target analysis by Beechem and coworkers [11–13], Ameloot et al. [14], Holzwarth [15] and Dioumaev [16]. These reviews demonstrate the importance of simultaneous (global) analysis of multiple decay traces. The combination of global analysis with testing of a photophysical or photochemical model is often called target analysis [11,15]. Reviews discussing global analysis in combination with experimental techniques are Refs. [1,17]. In addition, the BR photocycle has been a model system also for global and target analysis [18–22]. Recently five-way data (wavelength, time, temperature, polarization dependence, acidity) from this photocycle were subjected to a comprehensive target analysis [23]. In this paper, an

overview of the global and target analysis methodology will be given, emphasizing the need for modelling of both kinetics and spectra.

The word *model* is used here in two different ways. On the one hand, a model for the observations is formulated in mathematical-statistical terms. Thereby the measurements are described stochastically, since taking into account the noise properties is essential for precise parameter estimation [24,25]. On the other hand, the experimentalist is studying a complex system, generating a huge amount of observations. The goal of the experiment is to arrive at a simplified description of the system and estimate the essential physicochemical parameters with the help of a parameterized model. Most often such a model consists of a kinetic scheme containing transitions between states, which is also called a compartmental model. In this case the word *model* is used as a simplified description, and not in the above statistical sense. In Section 2 the assumptions regarding both the measurement process and the physicochemical model for the complex system which together lead to a model for the observations are discussed. The most important equations for global and target analysis are presented, and explained. The subsections of Section 2 describe aspects of particular building blocks for the final physicochemical model. These building blocks are tailored for the experiments to be modelled. Thus, a dynamic experiment usually requires a kinetic model, most often a compartmental model (Section 2.4.3). Taking into account the measurement conditions requires introduction of the instrument response function (IRF, Section 2.1.1). Extra building blocks are needed to describe, e.g. temperature dependence (Section 2.4.3.5) or anisotropy properties (Section 2.7.5). Still this is only a description of the temporal aspects of the data. Spectral model assumptions have to be added on top of this. This combination of kinetic and spectral model assumptions, discussed in Section 2.7, is most promising for the unravelling of complex systems. It enables estimation of crucial parameters like branching ratios, which can only be estimated because of the spectral model assumptions. Throughout Section 2 examples are described to illustrate the methods. The most relevant aspects of the parameter estimation are summarized in Section 3. In Section 4 an in-depth case study of ultrafast dynamics in PYP will be presented.

2. Model for the observations

2.1. Measurement process

A time-resolved spectrum is a collection of measurements done at different (distinct) times and wavelengths. Three measurement sequences can be distinguished:

(a) Measurements can be done simultaneously at a great number of wavelengths and at a certain time delay with respect to the exciting pulse. This is called a time gated spectrum. A collection of such time gated spectra at different time delays constitutes a time-resolved spectrum. With pump-probe spectroscopy, a time gated spectrum is susceptible to baseline fluctuations.
(b) Alternatively, at a particular wavelength a decay trace is measured as a function of time with respect to the exciting pulse. Again a collection of such decay traces measured at different wavelengths constitutes a time-resolved spectrum.
(c) Detection of decay traces at a great number of wavelengths simultaneously, providing high resolution in both dimensions, is possible with a (synchroscan) streak camera in combination with a spectrograph [26,27].

The three types of measurements require different preprocessing (e.g., baseline correction) and differ in their noise statistics. The resolution of the measurements is determined by a number of instrumental characteristics and by the stochastics of the measurements. Time resolution is limited by both the width of the exciting laser pulse and the width of the detector response. Wavelength resolution is determined by the characteristics of the spectrograph used. Below we discuss in some detail aspects of the measurement process.

2.1.1. The instrument response function

Usually the system is excited by a short laser pulse of a certain energy. The convolution of the shape of this exciting pulse and the detector response is called the IRF. The IRF limits the fastest response observable in the experiment. With pumpprobe spectroscopy the IRF is given by the convolution of pump and probe pulses. Ideally the IRF width should be shorter than the shortest time scale under study. This is impossible when studying ultrafast phenomena. On a (sub)picosecond time scale, the shape of the IRF as well as its timing precision become important.

Ideally the IRF should be measured once and for all with infinite precision, to avoid complications in the further analysis. In practice the problem can be tackled in different ways, depending upon the experimental technique. With fluorescence measurements there are three options: (a) The instrument response can be measured at the excitation wavelength (which is different from the emission wavelength) allowing for a wavelength-dependent time-shift parameter which needs to be estimated [28]. (b) The instrument response can be measured indirectly by adding a reference compound whose kinetic properties are known (reference convolution method, [29,30]). (c) A parameterized description of the instrument response can be included in the model function, leading to the necessity to estimate these extra parameters (Section 2.4.2).

A further complication with dispersed (sub)picosecond measurements is the dependence of the IRF upon the detection wavelength. This wavelength-dependent group velocity

delay (dispersion) can be described by a polynomial function for the IRF location parameter, of which the parameters must be estimated (from the data, or from a separate measurement, e.g. of the cross-phase modulation [31]).

2.1.2. Stochastics

The stochastics of spectroscopic measurements originate from photon properties. Single photon timing fluorescence measurements constitute a counting process which is Poisson distributed, where the variance is equal to the mean and all observations are independent. In contrast, the stochastic properties of the other types of measurements are much more uncertain. The observations are assumed to contain additive normally distributed noise. In general these observations are also assumed to be statistically independent, which seems justified because the measurements are done sequentially. There is one exception: with time gated spectra a whole spectrum is observed simultaneously, and in principle the responses measured at different wavelengths could be statistically dependent with (unknown) covariance matrix Σ (independent of time) [32]. With independent measurements there are several possible cases for the usually unknown variance σ^2 which may in principle depend upon time t and wavelength λ: (a) constant variance $\sigma^2(t, \lambda) = \sigma^2$ which is the most common assumption; (b) wavelength-dependent variance $\sigma^2(t, \lambda) = \sigma^2(\lambda)$ which is appropriate with difference absorption measurements. In general, $\sigma^2(\lambda)$ needs to be estimated as well. This procedure is called *iteratively reweighted least squares* [33]. (c) In addition to wavelength dependence, there may be time dependence $\sigma^2(t, \lambda)$, because the time interval of the measurement, and thus the signal to noise ratio, may increase with time [34]. (d) For large numbers of counts the abovementioned Poisson distributed single photon timing measurements are usually well approximated by a normal distribution with the variance equal to the mean.

2.2. Model assumptions

2.2.1. Homogeneity

A classical problem in describing reaction dynamics is (in)homogeneity [35,36]. The common assumption is that the properties of the system studied are homogeneous, which means that a discrete set of parameters describes the whole system. The observed dynamics of the ensemble can be ascribed to the dynamics of each individual member of that ensemble. In some cases there are indications that subpopulations are present [34,37] and it is assumed that such a system can be represented by a weighted average of homogeneous subsystems. When many subsystems are present, this can be described by a model with distributed parameters. A frequent discussion is the possibility to distinguish between models with discrete parameters and models with distributed parameters [39,40]. Biophysical knowledge of, e.g. a distribution of protein conformations, necessitates the use of models with distributed parameters. However, nearly all models used in practice lump parameters into a discrete set. An extra complication is that the two types of model can only be distinguished experimentally with very high signal to noise ratios, or when measurements are done over many orders of time, or as a function of temperature, or as a function of excitation wavelength.

Unless noted otherwise, we will assume that we are dealing with a homogeneous system which can be modelled with discrete parameters.

2.2.2. Separability

The spectroscopic properties of a mixture of components are a superposition of the spectroscopic properties of the components weighted by their concentration. With absorption this is known as the Beer–Lambert law. Thus, the noise-free, time-resolved spectrum $\psi(t, \lambda)$ is a superposition of the contributions of the n_{comp} different components:

$$\psi(t, \lambda) = \sum_{l=1}^{n_{\mathrm{comp}}} c_l(t)\varepsilon_l(\lambda) \tag{1}$$

where $c_l(t)$ and $\varepsilon_l(\lambda)$ denote, respectively, the concentration and spectrum of component l. Typical values for the number of components which can be studied with time-resolved spectroscopy are $1 \le n_{\mathrm{comp}} \le 10$, whereas both the number of different wavelengths and the number of different time instants can vary from n_{comp} to thousands.

Note that according to Eq. (1), a separability of time and wavelength properties is possible. However, with ultrafast measurements there is a caveat: the properties of the detector system are in general wavelength-dependent on a (sub)picosecond time scale (Section 2.1.1), thus with wavelength-dependent parameters θ (λ) the model for the concentration reads c_l (t, $\theta(\lambda)$). Regarding Eq. (1), we note that the quantity which will be estimated is the product ε_l which in itself is insufficient for the determination of the absolute values of c_l and ε_l. Thus, when we have, e.g. a kinetic model and no additional information, we can only identify the parameters which determine the shapes of c_l and ε_l. With a detailed kinetic model, sometimes the relative concentrations of the components can be estimated, and thus also the relative amplitudes of their spectra. We will return to this indeterminacy in Section 2.6.2.

2.3. Inverse problem

Measurement of ψ poses the inverse problem: how the spectroscopic and kinetic (dynamic) properties of the components can be recovered from the data. In practice various problems can arise: first, the number of components present in the system may be unknown. Second, in general neither the concentration profiles $c_l(t)$ nor the spectra $\varepsilon_l(\lambda)$ are known. However, the experimentalist usually has a priori knowledge about which shapes of concentration profiles or spectra are realistic. This amounts to common statements regarding continuity, nonnegativity,

Errata

page	column	line	old	new	remark
85	2	31	product ε_l	product $c_l\varepsilon_l$	please add c_l
85	2	34	and	for c_l and	please add "for c_l "
86	2	1	$\tilde{\Delta} = \Delta/(2\sqrt{\log(2)})$	$\tilde{\Delta} = \Delta/(2\sqrt{2\log(2)})$	please add 2 under sqrt
90	1	4	and $(\bar{\nu})$ is	and $f(\bar{\nu})$ is	please add *"f"*
90	1	14	(irreproducible)	$d\varepsilon(\bar{\nu})/d\bar{\nu} = 0$	this is a derivative
90	1	30	$\varepsilon\bar{\nu}$	$\varepsilon(\bar{\nu})$	add parentheses
90	2	36	$m \times n$	$m \times m$	note that U is a square matrix

unimodality, etc. A large amount of research is based upon such physical constraints in the self-modeling of two-way data [41,42]. Self-modeling was applied to the BR photocycle [43–45].

In many cases more knowledge is available in the form of a parameterized model for $c_l(t)$, termed a kinetic model (Section 2.4), or for $\varepsilon_l(\lambda)$, termed a spectral model (Section 2.5). Still, there may be several candidate kinetic models available, and dependencies in a kinetic model may render parameters unidentifiable. In the following two sections we present often well-known models in detail. In Section 2.6 a fundamental identiability problem is discussed. Finally in Section 2.7 the more powerful spectrotemporal models are introduced, which provide a solution to this problem.

2.4. Kinetic models

A first distinction to be made is the order of the kinetics. In case the concentrations are described by linear differential equations we are dealing with first order kinetics. The solution of a system of linear differential equations is given by a sum of exponential decays convolved with the IRF (Section 2.1.1). When the differential equations contain product of concentrations terms we are dealing with second order kinetics [46,47]. In the following, we will restrict ourselves to first order kinetics, but many aspects of these methods are also applicable with more complex kinetics.

2.4.1. Global analysis

Without a priori knowledge about a detailed kinetic model, the first step is to fit the data with a sufficient number of exponential decays and their amplitudes [48], which constitute the Decay Associated Spectra (DAS) [11,12,49–51]. Note that this number can be larger than the number of spectrally different components present. Subsequently, the DAS can be fitted with a spectral model [32]. DAS are most common with fluorescence or absorption spectroscopy. With *difference* absorption spectroscopy the amplitudes associated with exponential decays are termed Decay Associated Difference Spectra (DADS) [15]. When the IRF width is negligible the model reads $c_l(t) = \exp(-k_l t)$ with decay rate parameter k_l. Otherwise, as explained in Section 2.1.1, with ultrafast measurements the exponential decay has to be convolved with the IRF.

2.4.2. Convolution of exponential decay with IRF

Often the IRF $i(t)$ can be well described by a Gaussian with two parameters for the location (mean) μ and the full width at half maximum (FWHM) Δ:

$$i(t) = \frac{1}{\tilde{\Delta}\sqrt{2\pi}} \exp(-\log(2)(2(t-\mu)/\Delta)^2) \tag{2}$$

where $\tilde{\Delta} = \Delta/(2\sqrt{\log(2)})$. The convolution of this IRF with an exponential decay results in an analytical expression which facilitates the estimation of the IRF parameters μ and Δ (which is often necessary):

$$\begin{aligned} c(t;k,\mu,\Delta) &= \exp(-kt) \oplus i(t) \\ &= \frac{1}{2}\exp(-kt)\exp\left(k\left(\mu + \frac{k\tilde{\Delta}^2}{2}\right)\right)\left\{1 + \operatorname{erf}\left(\frac{t-(\mu+k\tilde{\Delta}^2)}{\sqrt{2}\tilde{\Delta}}\right)\right\} \end{aligned} \tag{3}$$

where the $\oplus$ indicates convolution. A complication arises with fluorescence measurements by a synchroscan streak camera [26] (Section 2.1c) because of additional contributions to Eq. (3) due to long-lived components [52].

With inhomogeneous kinetics (Section 2.2.1), a decay trace can be fitted with a parameterized distribution, for instance a Gaussian on the (natural) log (k) scale with location k_0 and width σ [40]:

$$\begin{aligned} &\int_{-\infty}^{\infty} \exp(-(\log(k) - \log(k_0))^2/(2\sigma^2)) \\ &\quad \times (\exp(-kt) \oplus i(t)) d\log(k) \end{aligned} \tag{4}$$

Alternatively, a nonparametric distribution of lifetimes (or decay rates) can be estimated. Fits of single traces with distributions of lifetimes [38] have been reviewed in [39], whereas lifetime density maps of time-resolved spectra have been presented in [53,54]. Subsequent target analysis can be performed on the kinetics obtained from the lifetime density maps [54]. A wavelength-dependent delay parameter μ is often used with single photon timing data to account for the wavelength dependence of the instrument response:

$$c(t;k,\ \mu) = \int_0^t \exp(-ks) i(t-s-\mu) ds \tag{5}$$

where now $i(t)$ represents the measured IRF. Note that the stochastic character of the measured IRF is neglected. A convolution algorithm for Eq. (5) is described in Ref. [55].

2.4.3. Compartmental models

When a priori knowledge about a detailed kinetic model is available, a linear time-invariant compartmental model [56,57] can be used. Because in contrast to global analysis, a specific kinetic model is tested, this is often termed target analysis [11,15,58,59]. The target here is to describe the real concentrations of the components. Note that the global analysis is equivalent to a number of noninteracting, parallelly decaying compartments. An important question is whether all unknown kinetic parameters can be estimated from the data. To answer this, a first step is of course detection of structural (un) identifiability [15,60], which is caused by incomplete information on the system. When different compartmental schemes result in the same model output, the system is structurally unidentifiable. But even a

structurally identifiable model may be numerically unidentifiable [57].

Transitions between compartments are described by microscopic rate constants which constitute the off diagonal elements of the transfer matrix K. The diagonal elements of K contain the total decay rates of each compartment. The concentrations of each compartment are described by a vector $c(t)=[c_1(t)\ldots c_{n_{\text{comp}}}(t)]^T$. Thus, a linear compartmental model with n_{comp} compartments is described by a differential equation for these concentrations:

$$\frac{d}{dt}c(t) = Kc(t) + j(t) \tag{6}$$

where the input to the system is described by a vector $j(t)=i(t)\ [1\ x_2\ \ldots\ x_{n_{\text{comp}}}]^T$, with $i(t)$ the IRF (Section 2.1.1) and x_l representing a possible extra input to compartment l. Eq. (6) can be solved analytically, which is important for both insight into the problem and for computational speed.

We assume that all eigenvalues of the transfer matrix K are different, and that $c(-\infty)=0$. The solution of Eq. (6) is then given by $c(t)=e^{Kt}\oplus j(t)$ where $\oplus$ indicates convolution. For a diagonal K-matrix ($K=\text{diag}(-k_1,\ldots,-k_{n_{\text{comp}}})$) with all inputs x_l equal to 1, the concentration matrix C consists of elements $[C_{\text{I}}]_{pq}=c_q^{\text{I}}(t_p,\ k_q)=\exp(-k_q t_p)\oplus i(t)$. The sub- or superscript I indicates that this is Model I comprising independently decaying compartments, also called parallel model.

For the evaluation of the exponential of a non-diagonal K matrix, we use the eigenvector-eigenvalue decomposition $K=U\Lambda U^{-1}$. With $\Lambda=\text{diag}(-k_1,\ldots,-k_{n_{\text{comp}}})$ we have $e^{Kt}=Ue^{\Lambda t}\,U^{-1}$ and

$$e^{Kt}\oplus j(t) = U\text{diag}\left(U^{-1}\left[1\ x_2\ldots x_{n_{\text{comp}}}\right]^T\right) \times \left[e^{-k_1 t}\oplus i(t)\ldots e^{-k_{n_{\text{comp}}} t}\oplus i(t)\right]^T \equiv A_{\text{II}}^T C_{\text{I}}^T \tag{7}$$

Thus, the solution of the general compartmental model is a linear combination of the c_l^{I} and thus a transformation of C_{I} (derived from the eigenvalues of the transfer matrix K) for which we can write

$$C_{\text{II}} = C_{\text{I}}A_{\text{II}} \tag{8}$$

with $A_{\text{II}}^T=U\text{diag}(U^{-1}[1\ x_2\ \ldots\ x_{n_{\text{comp}}}]^T)$.

Note that a compartmental model is closely related to the state space representation in mathematical systems theory,

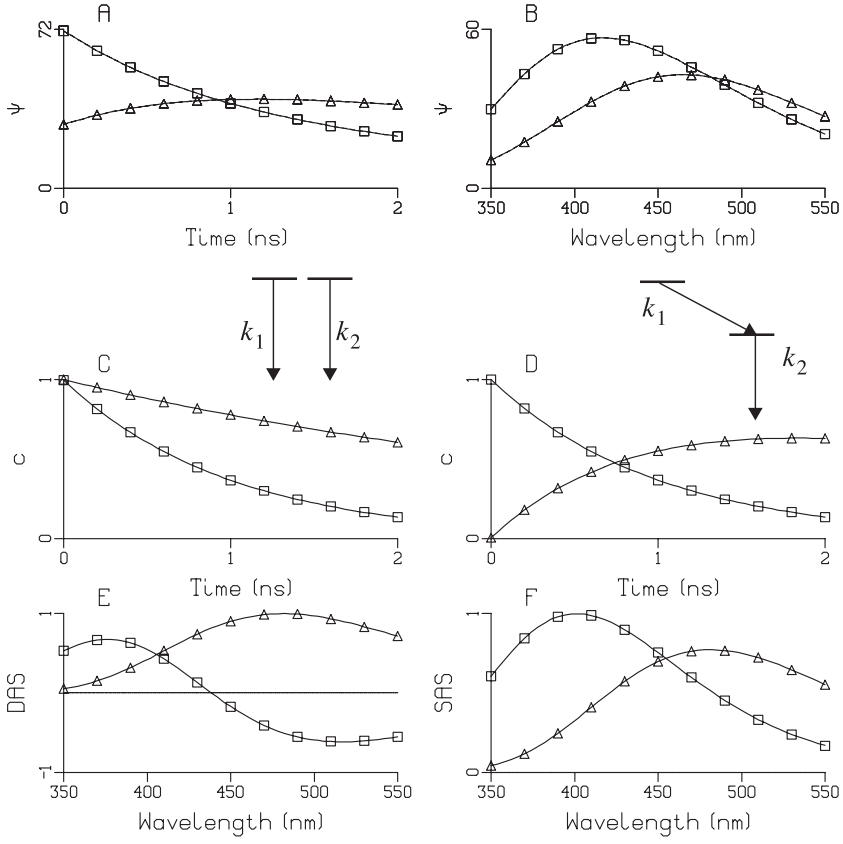

Fig. 1. Global analysis of simulated data from a two-compartment model with kinetic scheme $1\rightarrow 2$ (right inset). The first component (indicated by squares in panel D, F) decays in 1 ns, thereby forming the second component (indicated by triangles, life time 4 ns). (A) Decay traces at 400 and 500 nm (indicated by squares and triangles). (B) Time gated spectra at 0.4 ns (squares) and 1.6 ns (triangles). (C, E) $c(t)$ and estimated DAS using the incorrect parallel scheme 1|2 (left inset). (D, F) $c(t)$ and estimated SAS using the correct sequential scheme.

with the vector of concentrations of compartments being the state vector [61].

2.4.3.1. Simulation of a simple two-compartment model. To illustrate the previous section, a simple two-compartment model has been simulated, using realistic parameters [32]. In this model the first compartment, representing component 1, is excited. Component 1 irreversibly decays with rate k_1 thereby forming component 2 with fractional yield Φ_{12}. Component 2, which is represented by the second compartment, decays with rate k_2, which is smaller than k_1. This kinetic scheme is depicted in the right inset of Fig. 1, and the concentrations are shown in Fig. 1D. For this scheme the transfer matrix K is of lower triangular form:

$$K_{\mathrm{II}} = \begin{bmatrix} -k_1 & 0 \\ \Phi_{12}\ k_1 & -k_2 \end{bmatrix} \tag{9}$$

The subscript II indicates that this is Model II, which is abbreviated $1 \rightarrow 2$. Recall that Model I, which was defined in Section 2.4.3, consists of independently decaying compartments (which is abbreviated 1|2), and is depicted in the left inset of Fig. 1.

We now have for the matrix A_{II} of Eq. (8):

$$A_{\mathrm{II}} = \begin{bmatrix} 1 & -\alpha \\ 0 & \alpha \end{bmatrix} \quad A_{\mathrm{II}}^{-1} = \begin{bmatrix} 1 & 1 \\ 0 & \alpha^{-1} \end{bmatrix} \tag{10}$$

with $\alpha = \Phi_{12}k_1/(k_1 - k_2)$. A time-resolved (fluorescence or absorption) spectrum $\psi(t, \lambda)$ is simulated by a superposition of the concentrations of the components multiplied by their differing spectra (Fig. 1F) according to Eq. (1) (to improve readability we suppress here the time and wavelength dependence of $c_i(t)$, $\varepsilon_i(\lambda)$, respectively)

$$\psi = c_1^{\mathrm{II}}\varepsilon_1^{\mathrm{II}} + c_2^{\mathrm{II}}\varepsilon_2^{\mathrm{II}} \tag{11}$$

Typical traces and spectra are depicted in Fig. 1A and B. Now these simulated data can be fitted in two different ways, using Model I or II. When using Model II, with the correct kinetic scheme $1 \rightarrow 2$, and with $k_1 > k_2$, the estimated amplitudes associated with the concentrations c_l^{II} are called Species Associated Spectra (SAS) [11,49,51]. The estimated SAS in Fig. 1F are indistinguishable from the simulated component spectra $\varepsilon_l^{\mathrm{II}}$. By contrast, when these data are analysed using the incorrect kinetic scheme Model I with two independent decays c_l^{I}, the Decay Associated Spectra (DAS) $\varepsilon_l^{\mathrm{I}}$ depicted in Fig. 1E are estimated. Using Eqs. (8) and (10), we find $c_1^{\mathrm{II}} = c_1^{\mathrm{I}}$, $\varepsilon_1^{\mathrm{II}} = \varepsilon_1^{\mathrm{I}} + \varepsilon_2^{\mathrm{I}}$, $c_2^{\mathrm{II}} = \alpha(c_2^{\mathrm{I}} - c_1^{\mathrm{I}})$ and $\varepsilon_2^{\mathrm{II}} = \varepsilon_2^{\mathrm{I}}/\alpha$, which means that the differences between the two models are that the concentration of the formed component is proportional to the difference between the two decays, whereas the spectrum of the precursor is the sum of the two DAS (cf. Fig. 1E and F). The other way around, the DAS of the precursor is a linear combination of the SAS, $\varepsilon_1^{\mathrm{I}} = \varepsilon_1^{\mathrm{II}} - \alpha\varepsilon_2^{\mathrm{II}} (= \varepsilon_1^{\mathrm{II}} - \varepsilon_2^{\mathrm{I}}$, cf. Fig. 1E and F), thus it can contain negative amplitudes when the kinetics obey model II and the SAS overlap. Observation of negative amplitudes in a DAS indicates the presence of an (excited state) reaction [11], like in model II. This Model II has been successfully applied with bridged electron donor–acceptor systems where after excitation the charge-transfer state exhibits conformational dynamics, which can be observed by a red shift of the emission spectrum [32,62].

2.4.3.2. The unbranched, unidirectional model. Apart from the global analysis with independent decays $(1|2|\ldots|n_{\mathrm{comp}})$, the simplest kinetic scheme is the unbranched, unidirectional model $(1 \rightarrow 2 \rightarrow \ldots \rightarrow n_{\mathrm{comp}})$. These models are also termed parallel and sequential, and correspond to the generalization of the models I and II of the previous section. In the sequential model back-reactions are ignored on the assumption that the energy losses are large enough that the reverse reaction rates are negligible. Note the assumption that there are no losses in the chain $1 \rightarrow 2 \rightarrow \ldots \rightarrow n_{\mathrm{comp}}$. The compartmental model can be solved to yield [18]:

$$c_l(t) = \sum_{j=1}^{l} b_{jl}\exp(-k_j t) \oplus i(t) \tag{12}$$

where k_j is the decay rate of compartment j and the amplitudes b_{jl} of the (convolved) exponential decays are defined by $b_{11} = 1$ and for $j \leq l$:

$$b_{jl} = \prod_{m=1}^{l-1} k_m \Big/ \prod_{n=1}^{l}{}_{n \neq j}(k_n - k_j) \tag{13}$$

In particular, for $j < l$, $b_{j,l} = b_{j,l-1}k_{l-1}/(k_l - k_j)$. Of course, hybrids of the generalized models I and II, containing a mixture of parallelly and sequentially decaying compartments, can also easily be solved.

2.4.3.3. Multiexponential decays. Multiexponential decay of a component can originate from inhomogeneity (Section 2.2.1) or from equilibria. With equilibria, the number of compartments involved determines the degree of multiexponentiality. Take as an extreme case a model with just one emitting component P which is reversibly coupled to a number of other non-emissive states $h\nu \leftarrow P \leftrightarrow Q \leftrightarrow R$. When this three-compartmental system is excited, the decay of P shows a three-exponential decay. Since P is the only fluorescing component, its concentration profile is directly observed which offers possibilities for determining (relations between) the other rate constants in this intricately coupled system. Note that in this example only one component is observed, but three compartments are needed to describe its kinetics. The alternative kinetic scheme, $Q \leftrightarrow P \leftrightarrow R$, where the emissive state P is connected to non-emissive states Q and R, also results in three-exponential decay of P. Thus, when only P-emission is observed, the system is structurally unidentifiable. An example is the case

of the bacterial photosynthetic reaction centre, for which the emission from the excited primary donor P* is assumed to be in equilibrium with non-emitting relaxed radical pair states [63]. Such radical pair states are directly observed in transient absorption. In an elaborate target analysis of transient absorption from photosystem I reaction centres [54] many different kinetic schemes were considered. The final scheme describing the energy transfer and charge separation kinetics also contained an equilibrium between the excited primary donor and a radical pair. In turn, the primary donor is in equilibrium with two energy transferring antenna pigment pools. In this way, equilibria describe the four exponential decay of the two antenna pools, primary donor and radical pair state. These equilibria quantitatively describe the free energy differences in this complex system.

2.4.3.4. "Invisible" compartments. A compartment can be spectrally invisible, e.g. because the species represented by the compartment does not emit or absorb light. In difference absorption spectroscopy, compartments may possess indistinguishable spectral properties (giving rise to spectrally silent transitions [64]). Or there may exist linear relations between spectra of the compartments. Then the number of spectrally and temporally different components whose properties can be estimated will be less than the number of compartments. The C-matrix of these components can be obtained by postmultiplication in Eq. (8) of C_{I} by a modified A_{II}. Alternatively, this can be described by a spectrotemporal model using spectral equalities or constraints (see Section 2.7.2).

2.4.3.5. Measurements at different temperatures. The temperature dependence of microscopic rate constants can be described with a model containing thermodynamic parameters. Measurements at more different temperatures than the amount of unknown thermodynamic parameters will provide extra information. This offers an opportunity to identify and estimate both forward and backward microscopic rate constants [19,20], thus enabling estimation of free energy differences. In order to fit such measurements globally, a target analysis using a detailed compartmental model is mandatory. The temperature dependence of a microscopic rate constant k can be described in three different ways: by an Eyring relationship [19,23,35]

$$\ln(K^{\#}) = \frac{\Delta S^{\#}}{R} - \frac{\Delta H^{\#}}{RT} \tag{14}$$

where $K^{\#}=(kh)/(k_{\mathrm{B}}T)$ is the activation equilibrium constant and $\Delta S^{\#}$, $\Delta H^{\#}$ are the entropy, and enthalpy changes of activation. k_{B}, h, R are the Boltzmann, Planck and gas constants, respectively. Alternatively, an Arrhenius relationship

$$k = k_0 e^{-E_A/RT} \tag{15}$$

has been used, e.g. in modelling the BR photocycle [20]. To explain the anomalous temperature dependence of the recovery rate in the photoactive yellow protein photocycle, Van Brederode et al. [65] introduced a heat capacity change of activation parameter $\Delta C_p^{\#}$:

$$\ln\left(K^{\#}\right) = \frac{\Delta S^{\#}(T_0)}{R} - \frac{\Delta H^{\#}(T_0)}{RT} - \frac{\Delta C_p^{\#}}{R} \times \left(1 - \frac{T_0}{T} + \ln\left(\frac{T_0}{T}\right)\right) \tag{16}$$

where T_0 is a reference temperature.

2.5. Spectral models

When the spectral resolution of two-way spectral data is high, and an appropriate spectral model is available, analysis with a spectral model can be appropriate. In particular, when the time resolution is low, or when systematic errors like time jitter of time gated spectra (Section 2.1a) are present, global analysis using a spectral model is appropriate [62].

Spectral models are more phenomenological than kinetic models. In general, they require more parameters than a kinetic model. With difference absorption spectroscopy, the ground state spectrum can be included in the spectral model. Analogous to global analysis with single exponential decays, two-way spectral data can be analysed globally. Without a priori knowledge about detailed component spectra, the first step is to fit the data with a sufficient number of band shapes and their amplitudes, the band amplitude curves (BAC). With time-resolved spectra, subsequently the BAC can be fitted with a kinetic model [62]. With steady-state spectra measured as a function of temperature, subsequently the BAC can be fitted with a thermodynamic model [66]. When there are linear dependencies in the BACs, and the number of bands used is larger than the number of spectrally and temporally different components, a combination of (some of the) band shapes may lead to component spectra. This is analogous to the target analysis with compartmental models. Now the targets are the spectra of the real components.

2.5.1. Spectral shapes

The absorption spectrum for a homogeneously broadened (no inhomogeneity) transition can be well described by a Lorentzian band shape, whilst for an inhomogeneously broadened system (which is the case in most proteins and glasses), the corresponding spectrum is well described by a Gaussian [36,67]. Often times, the measured spectrum (both absorption and fluorescence) of an ensemble of chromophores can be deconvolved into a superposition of such bands, with specified spectral band shapes (e.g. Gaussian, Lorentzian, Voigt, skewed Gaussian, Pearson, ...). Thus, the shape of a spectrum of a component is assumed to be a superposition of such standard band shapes. Here we present model functions for the (skewed) Gaussian shape. The shape of a charge

transfer fluorescence emission spectrum is often well described by a Gaussian in the energy domain [68]: $f(\bar{\nu})/\bar{\nu}^3 = f_{\max}\exp(-\ln 2[2(\bar{\nu}-\bar{\nu}_{\max})/\Delta\bar{\nu}]^2)$ where $\bar{\nu}=\lambda^{-1}$ denotes the wave number and $(\bar{\nu})$ is the converted fluorescence emission spectrum: $f(\bar{\nu})=\lambda^2\varepsilon(\lambda)$ [69]. Even better fits are achieved when an extra skewness parameter is introduced [70,71]. Thus, we arrive at the model function [32]

$$\varepsilon(\bar{\nu}) = \bar{\nu}^5 f_{max}\exp(-\ln 2[\ln(1+2b(\bar{\nu}-\bar{\nu}_{max})/\Delta\bar{\nu})/b]^2) \tag{17}$$

Note that with skewness parameter $b=0$ the exponent in Eq. (17) reduces to a Gaussian (since $\lim_{b\to 0}(\ln(1+bx))/b = x$). The maximum of Eq. (17) in the wavelength domain is given by the numerical solution of the nonlinear equation $((d)/(d\bar{\nu}))\varepsilon(\bar{\nu})/d\bar{\nu}=0$. The Full Width at Half Maximum is given by $\Delta\bar{\nu}_{1/2}=\Delta\bar{\nu}\sinh(b)/b$.

Analogously the shape of a charge transfer absorption spectrum is often well described by a Gaussian in the energy domain [68]: $f(\bar{\nu})/\bar{\nu}=\varepsilon_{\max}\exp(-\ln 2[2(\bar{\nu}-\bar{\nu}_{\max})/\Delta\bar{\nu}]^2)$. When the vibronic coupling, quantified as a Huang–Rhys factor, between the chromophore and its vibrations is smaller than the magnitude of phonon–chromophore coupling, the resulting absorption spectrum can be well described as a Gaussian [72]. Even when the two are comparable, the introduction of a skewness degree of freedom to the Gaussian can satisfactorily account for increased vibronic coupling. This leads to the model function:

$$\varepsilon(\bar{\nu}) = \bar{\nu}\varepsilon_{\max}\exp(-\ln 2[\ln(1+2b(\bar{\nu}-\bar{\nu}_{\max})/\Delta\bar{\nu})/b]^2) \tag{18}$$

In modelling an absorption difference spectrum the ground state spectrum ε_0 is subtracted from a linear combination of $\varepsilon\bar{\nu}$ as in Eq. (18):

$$\begin{aligned}\varepsilon(\bar{\nu};(\bar{\nu}_{\max},\ \Delta\bar{\nu},\ b)_1,\ldots,(\bar{\nu}_{\max},\Delta\bar{\nu},\ b)_M,\ a_1,\ldots,a_M)\\ = \sum_{m=1}^{M} a_m\bar{\nu}\exp(-\ln 2[\ln(1+2b_m(\bar{\nu}-\bar{\nu}_{\max,m})\\ /\Delta\bar{\nu}_m)/b_m]^2) - \varepsilon_0\end{aligned} \tag{19}$$

Note that analogous to the convolution with the measured instrument response, Eq. (5), the stochastic character of this measured ground state spectrum is neglected.

2.6. Model for the observations in matrix notation

In many cases the data can be collected in a matrix Ψ of dimensions $m\times n$, where m and n are, respectively, the number of different time instants and wavelengths. The matrix element ψ_{ij} then contains the measurement at time instant t_i and wavelength λ_j. Using the matrix notation greatly simplifies the description of the model for the observations and allows the use of matrix decomposition techniques (Section 2.6.1). Assuming additive noise (Section 2.1.2), the basic model which describes the time evolution of spectra is the following:

$$\underline{\psi}_{t_i\lambda_j} = \sum_{l=1}^{n_{\text{comp}}} c_{lt_i}\varepsilon_{l\lambda_j} + \underline{\xi}_{t_i\lambda_j} \tag{20}$$

c_{lt_i} denotes the concentration of component l at time t_i, $\varepsilon_{l\lambda_j}$ denotes the contribution of component l at wavelength λ_j, and $\underline{\xi}_{t_i\lambda_j}$ denotes a normally distributed stochastic disturbance with zero mean (the underlining indicates that a variable is stochastic). The c_{lt_i} and $\varepsilon_{l\lambda_j}$ are collated in the matrices C and E, of dimension $m\times n_{\text{comp}}$ and $n\times n_{\text{comp}}$, respectively. The columns of C are the concentration profiles of the components, whereas the columns of E are the component spectra. Note that possible systematic errors are not included in this description (see Section 2.1). When there is a wavelength-dependent time delay, we have

$$\underline{\psi}_{\lambda_j} = C\varepsilon_{\lambda_j} + \underline{\xi}_{\lambda_j} \tag{21}$$

and else we can write

$$\underline{\Psi} = CE^T + \underline{\Xi} \tag{22}$$

Matrix $\underline{\Xi}$ represents the noise and is, like Ψ, $m\times n$. ψ_{λ_j} and ξ_{λ_j} are the λ_j^{th} column of, respectively, Ψ and $\underline{\Xi}$. ε_{λ_j} is the transpose of the λ_j^{th} row of E.

2.6.1. Estimation of the number of components

When there are no linear dependencies between the component spectra, and thus no linear relationships between the columns of E, the matrix E is of full rank. Analogously, when there are no linear dependencies between the concentrations of the components, and thus no linear relationships between the columns of C, the matrix C is also of full rank. This rank is equal to the number of components. Consequently, when rank (C) = rank (E) = n_{comp} and with noise-free data ($\underline{\Xi}=0$), we have rank (Ψ) = rank (CE^T) = n_{comp}. Thus, with experimental data of which we do not know the number of components, we can estimate this number by estimating the rank of $\underline{\Psi}$ using the Singular Value Decomposition [73–79] of $\underline{\Psi}$

$$\underline{\Psi} = \underline{U}\ \underline{S}\ \underline{W}^T \tag{23}$$

where U and W are orthogonal matrices, respectively, $m\times n$ and $n\times n$, whose columns contain the left and right singular vectors. S is an $m\times n$ matrix which is zero except for its diagonal, which contains the singular values. With n_{comp} components and noise-free data we have exactly n_{comp} significant singular values: $s_1\geq s_2\geq\ldots\geq s_{n_{\text{comp}}}>s_{n_{\text{comp}}+1}=\ldots=0$. The addition of the noise $\underline{\Xi}$ perturbs the SVD of the noise-free Ψ in two respects. First, the singular values are changed. According to Corollary 8.3.2. of Ref. [73], an upper bound for this perturbation is given by the largest singular value of $\underline{\Xi}$, say $s_{1,\underline{\Xi}}$. Thus, the perturbation is negligible when $s_l - s_{l+1} \gg s_{1,\underline{\Xi}}$, $l=1,\ldots,n_{\text{comp}}$. Second, the singular vector pairs (u_l, w_l), (u_{l+1}, w_{l+1}), are perturbed. Theorem

8.3.5. of Ref. [73] states that the amount of the perturbation depends upon the isolation of the relevant singular values. Thus, when $s_l - s_{l+1} \approx s_{1,\Xi}$, the noise can greatly alter the singular vector pairs.

When Eq. (22) is applicable, the number of components can be determined from the number of singular vector pairs and accompanying singular values significantly different from noise. The consequences of a wavelength-dependent time delay upon the rank are unclear, and need to be considered case by case.

2.6.2. Equivalence of spectral or kinetic models

Let us assume in the following that we have successfully determined n_{comp}. Starting from Eq. (22), we here distinguish two different kinds of parametrizations:

The concentrations are described by a kinetic model, which depends upon the parameters θ

$$\underline{\Psi} = C(\theta)E^T + \underline{\Xi} \tag{24}$$

The spectra are described by a parametric model, which depends upon the parameters θ

$$\underline{\Psi} = CE^T(\theta) + \underline{\Xi} \tag{25}$$

Subsequently, the estimated matrices E from Eq. (24) and C from Eq. (25) can be fitted with, respectively, a spectral and a kinetic model.

Because of the linearity of the model function, the decomposition of Ψ into the product of two matrices is problematic, which is to a differing extent recognized by many authors (e.g. Refs. [11,18,19,49,78,80–82]). Let A be an invertible matrix then:

$$CE^T = CAA^{-1}E^T = (CA)(EA^{-T})^T \tag{26}$$

Because we are dealing with a model function CE^T the linear combinations of spectral or kinetic models will produce the identical residual matrix $Z = \Psi - CE^T$. Thus, the minimum of the least squares criterion is independent of the details of the kinetic model as are the estimated kinetic parameters. From Eq. (26) we conclude that the difference between two kinetic models lies in their spectral parameters. A priori knowledge about E (for instance nonnegativity of the $\varepsilon_l(\lambda)$) offers us the possibility to choose between alternative models. With a spectral model an analogous problem exists, in this case the estimated concentrations need to be nonnegative. Summarizing: when no a priori information about the correct model is present, two steps must be distinguished in the analysis of time-resolved spectra: fitting the data and finding the "best" model. A common procedure is the following: exponential decays are assumed to be present and the data are fitted with a sufficient number of decays n_{decay}, so that the residuals appear satisfactory. This is usually termed "global analysis" (Section 2.4.1). Judging goodness of fit is strongly problem-dependent. Suppose the Decay Associated Spectra are all different (which is often the case), and the SVD analysis is in accordance with the presence of n_{decay} spectrally and temporally independent components. Note that in general the DAS do not correspond to real spectra, this is only the case when a component decays without interconversions to other (spectrally active) components. Then, to find the best compartmental model (Section 2.4.3), several models with $n_{\text{comp}} = n_{\text{decay}}$ components can be tried, comparing them by the plausibility of their then called Species Associated Spectra (SAS). Here a spectral model can be of great help. This is usually termed "target analysis". Furthermore, thermodynamic considerations can be helpful in case the dependence on temperature or pH has been measured (Section 2.4.3.5).

2.6.3. Projecting the data upon singular vectors

In Refs. [76,78] applications of SVD in time-resolved spectroscopy are discussed. SVD is also instrumental in self-modeling of the BR photocycle [43–45]. Next to the use of SVD for rank estimation (Section 2.6.1), an important application is data reduction and noise suppression. Assuming the noise is small, the Singular Value Decomposition results can be used to project the data upon the first n_{comp} singular vectors. Projecting upon the first n_{comp} right singular vectors the kinetic model Eq. (24) becomes

$$\underline{\Psi}W_{n_{\text{comp}}} = C(\theta)E^T W_{n_{\text{comp}}} + \underline{\Xi}W_{n_{\text{comp}}} \tag{27}$$

Analogously, projecting upon the first left singular vectors the spectral model Eq. (25) becomes

$$U^T_{n_{\text{comp}}}\underline{\Psi} = U^T_{n_{\text{comp}}}CE^T(\theta) + U^T_{n_{\text{comp}}}\underline{\Xi} \tag{28}$$

These projections reduce the dimensionality of the nonlinear least-squares fits [32,47,83,84], thus saving computational resources. A drawback of the projection is that the noise can easily perturb the projected data (Section 2.6.1), resulting in loss of information. Furthermore, it becomes much more difficult to calculate summary statistics (Section 3). These drawbacks can easily be avoided by using the variable projection algorithm [85], discussed more fully in Section 3, by which the nonlinear least-squares fit of the full, unprojected data becomes feasible.

2.7. Spectrotemporal models

In the ideal case all a priori knowledge is used for a model-based fit of the data. This leads to a spectrotemporal model [62]. Three cases can be distinguished: (1) a parameterized model for both kinetics and spectral shapes is available; (2) in addition to the kinetic model, limited spectral knowledge is available, in the form of spectral equalities or constraints (e.g. the spectrum is assumed to be zero in a certain wavelength range); and (3) in addition to the model for the spectral shapes, limited band amplitude

curve knowledge is available, e.g. a certain amplitude is assumed to be zero in a certain time range.

When the separability of time and wavelength properties, Eq. (1), is not applicable, sometimes a spectrotemporal model can be used [86,87]. E.g., in describing solvation, the time dependence of the spectral parameter $\bar{\nu}_{\max}$ from Eq. (17) or Eq. (18) can be described as $\bar{\nu}_{\max}(t) = \bar{\nu}_{\max}(\infty) + (\bar{\nu}_{\max}(0) - \bar{\nu}_{\max}(\infty))\exp(-t/\tau)$ where τ represents the characteristic solvation time.

2.7.1. Spectral shape model and kinetic model

The most straightforward spectrotemporal model includes a kinetic model (e.g. a compartmental model from Section 2.4.3), a spectral shape model (e.g. from Section 2.5.1) and in general also some amplitude parameters. In case both the kinetic and the spectral model are of a global type, these are the amplitudes of each combination of exponential decay and band shape. With a more detailed model they can be limited to one or more scaling parameters. It is shown in Ref. [88] that with such a detailed model, the parameters of a multicomponent model can be estimated with higher precision. In the case of zero spectral overlap, this precision is equal to the precision of a single component model.

In Eq. (29) both the concentrations and the spectra are described by a model, which depends upon the parameters θ. Assuming first order kinetics, a matrix of amplitude parameters A describes the concentrations of the components in terms of a superposition of simple decays which are collated in the matrix C(θ).

$$\underline{\Psi} = C(\theta)AE^T(\theta) + \underline{\Xi} \tag{29}$$

When applied to the simulated data of Section 2.4.3.1, the matrix $C(\theta)$ contains two exponential decays (parameters k_l), whereas the matrix $E(\theta)$ consists of two skewed Gaussian shapes (Eq. (17), parameters $(\bar{\nu}_{\max}, \Delta\bar{\nu}, b)_l$). The matrix of amplitude parameters A to be estimated will be proportional to the A_{II} from Eq. (10).

The vector representation [24] of the matrix Ψ is given by

$$\mathrm{vec}(\underline{\Psi}) = (E(\theta) \otimes C(\theta))\mathrm{vec}(A) + \mathrm{vec}(\underline{\Xi}) \tag{30}$$

where $\otimes$ denotes the Kronecker product [24]. In case a particular kinetic model (with concentrations $c_i(\theta)$) is tested, we put

$$\mathrm{vec}(\underline{\Psi}) = \sum_{i=1}^{n_{\mathrm{comp}}} \mathrm{vec}(c_i(\theta)\varepsilon_i^T(\theta))a_i + \mathrm{vec}(\Xi) \tag{31}$$

When applied to the simulated data of Section 2.4.3.1, this is equivalent to the target analysis with the c_i (θ) from Model II. Instead of the n_{comp}^2 parameters of the A matrix now only n_{comp} amplitude parameters need to be estimated. It was demonstrated in Ref. [88] that this improves the precision of the parameters θ in Eq. (31) relative to Eq. (30).

2.7.2. A priori spectral knowledge and kinetic model

The second type of spectrotemporal model includes a kinetic model (e.g. a compartmental model from Section 2.4.3), and a spectral model which incorporates limited a priori spectral knowledge, e.g. a spectrum is assumed to be zero in a certain wavelength range. Thus, in that wavelength range a component with zero spectrum does not contribute. An extreme case is the emission from P* (from the bacterial reaction centre) which is assumed to be in equilibrium with non-emitting relaxed radical pair states (see Section 2.4.3.3) [63]. With difference absorption measurements the situation becomes even more complicated, because the ground state bleach spectrum is needed as well, and in the case of a photocycle an extra parameter for the fraction cycling has to be introduced (Section 2.7.4).

The kinetic model of Eq. (24) needs to be modified in order to incorporate the a priori spectral knowledge

$$\underline{\Psi} = C(\theta)\tilde{E}^T + \underline{\Xi} \tag{32}$$

where $\tilde{E}^T$ contains less unknown parameters than $n \times n_{\mathrm{comp}}$. E.g. in a certain wavelength range for certain components some of the elements of $\tilde{E}$ are equal to zero, or some linear relationships exist. Examples will be discussed in Section 2.7.4 and in the case study (Section 4).

2.7.3. A priori band amplitude knowledge and spectral model

The third type of spectro"temporal" model includes a spectral shape model (e.g. from Section 2.5.1) and a BAC model which incorporates a priori knowledge, e.g. that in a certain time (or pH, or temperature, ...) range the band amplitude is assumed to be zero. Thus, in that range a component with zero amplitude does not contribute.

The spectral model of Eq. (25) needs to be modified in order to incorporate the a priori band amplitude knowledge

$$\underline{\Psi} = \tilde{C}E^T(\theta) + \underline{\Xi} \tag{33}$$

where $\tilde{C}$ contains less unknowns than $m \times n_{\mathrm{comp}}$. E.g. in a certain range for certain components some of the elements of $\tilde{C}$ are equal to zero, or some linear relationships exist. This type of model was applied in studying the oligomerization of photosynthetic antenna peptides [89]. From a series of detergent-dependent absorption spectra an intermediate spectrum could be resolved with the help of the constraints that this spectrum did not contribute at the extreme detergent concentrations.

2.7.4. Spectrotemporal model for a photocycle

With difference absorption measurements from a photocycle the situation becomes even more complicated, because the ground state bleach spectrum is needed as well, and an extra parameter for the fraction cycling has to be introduced.

The noise-free, time-resolved difference absorption ΔA is a superposition of the n_{comp} contributions of the different components (analogous to Eq. (1)):

$$\Delta A(t,\lambda) = \sum_{l=1}^{n_{\mathrm{comp}}} c_l(t)\Delta\varepsilon_l(\lambda) \tag{34}$$

where $c_l(t)$ and $\Delta\varepsilon_l(\lambda)$ denote, respectively, the concentration and SADS of component l. By definition, $\Delta\varepsilon_l(\lambda) = \varepsilon_l(\lambda) - \varepsilon_0(\lambda)$, where $\varepsilon_0(\lambda)$ is the ground state bleach spectrum. Regarding Eq. (34), we note that the quantity which will be estimated is the product $c_l\Delta\varepsilon_l$, which in itself is insufficient for the determination of the absolute values of c_l and $\Delta\varepsilon_l$. Since in the photocycle no states are lost, the relative concentrations of the components can be estimated, and thus also the relative amplitudes of their difference spectra. Here we take $c_1(0) \equiv 1$, and thus all concentrations are relative to the concentration of the first photocycle state in the model.

In matrix notation Eq. (34) reads:

$$\Delta A = C(E - \varepsilon_0)^T = CE^T - C1\varepsilon_0^T \tag{35}$$

where the $m \times n$ matrix ΔA denotes the time-resolved difference absorption, measured at m time instants t_i, and n wavelengths λ_j. The columns of the matrices C and E, of dimension $m \times n_{\mathrm{comp}}$ and $n \times n_{\mathrm{comp}}$, respectively, contain the concentration profiles and SAS of the components. The matrix–vector product $C1$ is a vector containing the sum of the concentrations of the photocycling intermediates, which is equal to the ground state depletion. This sum decreases monotonically from one at time zero to zero at the end of the photocycle. When the ground state spectrum of the sample before excitation $\tilde{\varepsilon}_0$ has been measured on exactly the same setup (which is not always feasible in the case of ultrafast measurements), the model can be extended with the fraction cycling parameter fc. We can then substitute for the bleach spectrum $\varepsilon_0 = fc \cdot \tilde{\varepsilon}_0$. Using the vector representation of a matrix and the Kronecker product [24] ($\otimes$), Eq. (35) can then be rewritten:

$$\mathrm{vec}(\Delta A) = (I_n \otimes C)\mathrm{vec}(E^T) - (\tilde{\varepsilon}_0 \otimes C1)fc \tag{36}$$

When we use a kinetic model, we can express Eq. (36) as

$$\mathrm{vec}(\Delta A) = [I_n \otimes C(\theta) - \tilde{\varepsilon}_0 \otimes C(\theta)1]\begin{bmatrix}\mathrm{vec}(E^T)\\ fc\end{bmatrix} \tag{37}$$

Since the last column $-\tilde{\varepsilon}_0 \otimes C(\theta)\,1$ is a linear combination of all the other columns, an extra assumption is necessary to remove this dependence. With BR the M state(s) are assumed not to absorb above $\approx$ 540 nm [23], thus removing these elements from $\mathrm{vec}(E^T)$ (arriving at $\mathrm{vec}(\tilde{E}^T)$) and deleting the accompanying columns in $I_n \otimes C(\theta)$. With photoactive yellow protein [6,91,92] the pB state(s) are assumed not to absorb above $\approx$ 430 nm. Both the M and pB states possess an absorption maximum to the blue of the ground state, and occur on a millisecond time scale during the photocycle.

2.7.5. Anisotropy models

Measurement and subsequent modelling of polarization dependence offer an opportunity to resolve components provided their anisotropies differ. Commonly measurements are made at three angles relative to the polarization of the excitation: parallel, perpendicular and magic angle. At the magic angle there is no anisotropy effect present, from the two other measurements the anisotropies can be estimated. In an associative model, an anisotropy decay function $r_i(t)$ is associated with each component i. Alternatively, a single anisotropy $r(t)$ can be applied to all components or to all decays, which is called a nonassociative model. The models discussed below are all associative.

2.7.5.1. Emission anisotropy. In order to include parallel and perpendicular data, the kinetic model for the magic angle data from Eq. (24) is extended by multiplying the concentration of each component i by $1 + \gamma r_i(t)$, where γ equals 0, 2, -1 for magic angle, parallel, and perpendicular data, respectively [12]. The full model for the experimental traces MA(t), VV(t), and VH(t) then reads:

$$\begin{bmatrix}\mathrm{MA}(t,\ \lambda)\\ \mathrm{VV}(t,\ \lambda)\\ \mathrm{VH}(t,\ \lambda)\end{bmatrix} = \left(\sum_{l=1}^{n_{\mathrm{comp}}} c_l(t)\varepsilon_l(\lambda)\begin{bmatrix}1\\ 1 + 2r_l(t)\\ 1 - r_l(t)\end{bmatrix}\right) \oplus i(t) \tag{38}$$

When Raman scattering is present, it can easily be included in the model. It has the time profile of the IRF and possesses an anisotropy r_{RS}, a spectrum $\varepsilon_{\mathrm{RS}}(\lambda)$, and contributes a term $\varepsilon_{\mathrm{RS}}(\lambda)(1 + \gamma r_{\mathrm{RS}})i(t)$ to Eq. (38). Ideally r_{RS} equals 0.4.

Preferentially the measured data are modelled in Eq. (38). Alternatively, an anisotropy signal can be calculated from the parallel and perpendicular data

$$r(t,\lambda) = \frac{\mathrm{VV}(t,\lambda) - \mathrm{VH}(t,\lambda)}{\mathrm{VV}(t,\ \lambda) + 2\mathrm{VH}(t,\lambda)} \tag{39}$$

Compared to the measured data, the calculated $r(t, \lambda)$ will be much more noise-sensitive, in particular when the signals are small.

2.7.5.2. Difference absorption anisotropy. With difference absorption the situation is much more complicated. An excited state component possesses three spectral contributions: excited state absorption (ESA), ground state bleaching

(GSB) and stimulated emission (SE), whereas a component in the ground state possesses two spectral contributions: absorption (GSA), and bleaching (GSB). In principle, each contribution has its own anisotropy. Thus, the total contribution of an excited state component reads (omitting the subscript l for clarity):

$$(c(t)\{\mathrm{ESA}(\lambda)(1+\gamma r_{\mathrm{ESA}}(t))+\mathrm{SE}(\lambda)(1+\gamma r_{\mathrm{SE}}(t)) + \mathrm{GSB}(\lambda)(1+\gamma r_{\mathrm{GSB}}(t))\})\oplus i(t) \quad (40)$$

whereas a ground state component contributes:

$$(c(t)\{\mathrm{GSA}(\lambda)(1+\gamma r_{\mathrm{GSA}}(t)) + \mathrm{GSB}(\lambda)(1+\gamma r_{\mathrm{GSB}}(t))\})\oplus i(t) \quad (41)$$

An important question is, under which conditions can these different contributions be resolved. Consider the following case: a ground state component possesses two contributions: a bleach with maximum anisotropy $r_{\mathrm{GSB}}=0.4$, and absorption. Suppose the bleach is not present in part of the measured wavelength range, then from that part r_{GSA} can be estimated from

$$\begin{bmatrix}\Delta A(t,\lambda)\\ \Delta A_{\parallel}(t,\lambda)\\ \Delta A_{\perp}(t,\lambda)\end{bmatrix} = \left(c(t)\mathrm{GSA}(\lambda)\begin{bmatrix}1\\ 1+2r_{\mathrm{GSA}}(t)\\ 1-r_{\mathrm{GSA}}(t)\end{bmatrix}\right)\oplus i(t) \quad (42)$$

When the thus estimated r_{GSA} differs from r_{GSB}, the two contributions can be resolved over the full wavelength range. In conclusion: contributions with different anisotropy can in principle be resolved when their anisotropy is known a priori, or when a contribution with unknown anisotropy appears isolated in part of the measurement range.

A coherent coupling artefact, which is often present in ultrafast experiments [31,93], can be included in the model. Usually its time profile can be approximated by the IRF. It possesses an anisotropy r_{CA}, a spectrum $\varepsilon_{\mathrm{CA}}(\lambda)$, and contributes a term $\varepsilon_{\mathrm{CA}}(\lambda)(1+\gamma r_{\mathrm{CA}})\ i(t)$ to Eq. (42). Target analysis of ultrafast difference absorption spectra was instrumental in resolving structural heterogeneity of the 2-aminopurine chromophore [90]. The different excited states possessed widely differing anisotropies, which were also wavelength-dependent. About 70% of the population showed a high anisotropy ($r\approx 0.35$) below 440 nm, and a low anisotropy ($r\approx 0.1$) above 440 nm. The remaining 30% of the population showed an opposite anisotropy ($r\approx -0.2$). The anisotropy information was limited to the first 50 ps, due to the rotational correlation time $\tau\approx 25$ ps of the chromophore, $r_i(t)=r_{0i}\exp(-t/\tau)$.

2.7.5.3. Anisotropy model for the BR photocycle. In Section 2.7.4 a general photocycle model was introduced. Here we extend this model with an anisotropy model for a special case, the BR photocycle. In order to include the parallel and perpendicular data, we extend the model for the magic angle photocycle data from Eq. (36) by multiplying the concentration of each component i (ground state bleaching (GSB) or photocycle intermediates) by $1+\gamma r_i(t)$, where γ equals 2, -1 for parallel and perpendicular data, respectively. The full model then reads [23]:

$$\begin{bmatrix}\Delta A(t,\lambda)\\ \Delta A_{\parallel}(t,\lambda)\\ \Delta A_{\perp}(t,\lambda)\end{bmatrix} = \sum_{l=1}^{n_{\mathrm{comp}}} c_l(t)\varepsilon_l(\lambda)\begin{bmatrix}1\\ 1+2r_l(t)\\ 1-r_l(t)\end{bmatrix} - fc \cdot \tilde{\varepsilon}_0\begin{bmatrix}1\\ 1+2r_{\mathrm{GSB}}(t)\\ 1-r_{\mathrm{GSB}}(t)\end{bmatrix}\sum_{l=1}^{n_{\mathrm{comp}}} c_l(t) \quad (43)$$

For the time dependence of the anisotropy, an exponential decay model can be used:

$$r_i(t)=r_{0i}\exp(-k_{\mathrm{tumb}}t) \quad (44)$$

in which k_{tumb} is the rate of (membrane) tumbling, and r_{0i} is the anisotropy at time zero of component i. An alternative method for target analysis of BR photocycle anisotropy data has been developed by Borucki et al. [94] and Heyn et al. [95]. Based upon mild assumptions, they exploited the anisotropy dimension to estimate the SAS and concentration profiles.

Lozier et al. [20] measured five-way data of the BR photocycle: wavelength from 380 to 700 nm, time from 1 μs to 0.3 s, temperature from 5 to 35 °C, under four solvent conditions (pH 5, pH 7, pH 9, and pD 7) and under three polarization conditions (magic angle, parallel and perpendicular). A spectrotemporal model was applied to these data [23], which consisted of five parts: (i) a compartmental scheme (Section 2.4.3) for the MA concentrations with fully reversible transitions between the photocycle intermediates (Fig. 2A), (ii) the temperature dependence of the microscopic rate constants was described with thermodynamic parameters (Eq. (14), Section 2.4.3.5) for each of the solvent conditions, (iii) a photocycle model (Eq. (37), Section 2.7.4) which contains the SAS including the GSB and a fraction cycling parameter. The SAS are assumed to be temperature independent [96], (iv) an anisotropy model (Eqs. (43) and (44)), and (v) spectral assumptions (Section 2.7.2) on the SAS, i.e. that the M intermediates did not absorb above 540 nm, that the N and O intermediates did not contribute to the difference absorption below 460 nm, and that the L and N intermediates did not absorb above 680 nm. Relative to the

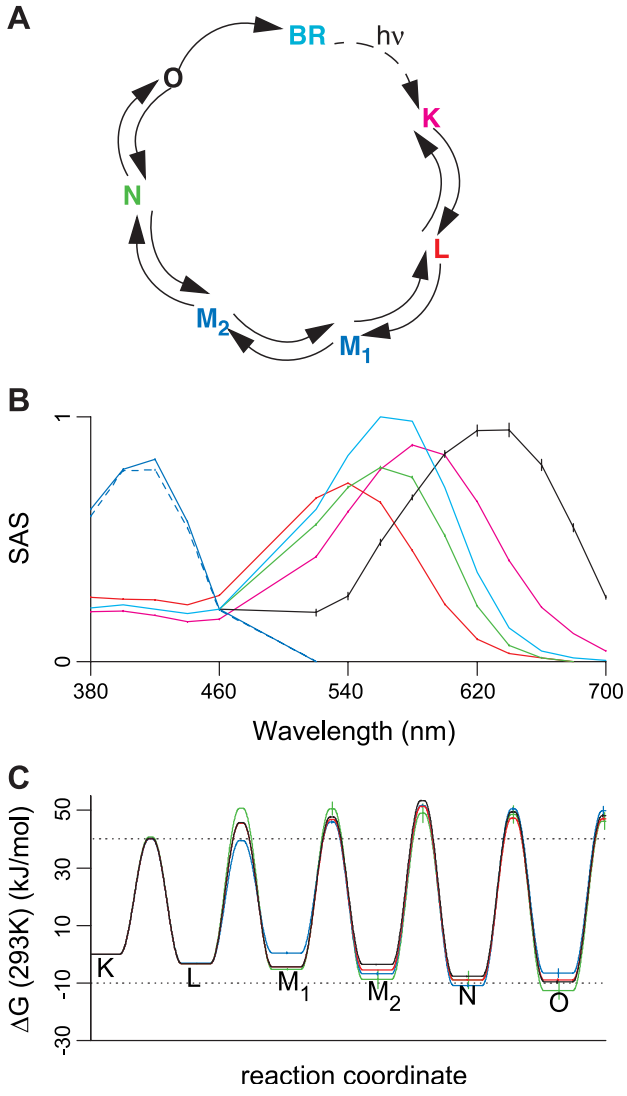

Fig. 2. Target analysis of bacteriorhodopsin photocycle, using a reversible compartmental scheme (A) with six intermediates K⇌L⇌M1⇌M2⇌N⇌O→BR. (B) Estimated SAS, note the congestion of K, L, N and BR. Key: magenta, K; red, L; blue, M; green, N; black, O; and cyan, BR. (C) Free energy changes relative to K (at 293 K) during the photocycle. Key: black, pH 5; red, pH 7; blue, pH 9; green, pD 7. Vertical bars indicate plus or minus standard error.

analysis in [20], parts (iii) and (v) were the major improvements. This model consistently described the five-way data. The estimated SAS are shown in Fig. 2B. From the thermodynamic parameters, the free energy changes during the photocycle can be calculated, and ΔG relative to the first intermediate is depicted in Fig. 2C. Thus, this target analysis is instrumental in monitoring the energetics of the BR photocycle. Although this photocycle has been studied for 30 years, there is still some controversy [21–23]. In an alternative approach, all possible kinetic schemes using a full K-matrix (Eq. (6)) were tested [19], successively eliminating superfluous microscopic rate constants. The method was tested on concentration profiles estimated from resonance Raman data, and arrived at a similar kinetic scheme [80], except for a few small differences. An alternative description with two parallel, irreversible photocycles is proposed in [21,22]. This exemplifies that the explanation of multiexponential decay of components by equilibria or by heterogeneity (Section 2.4.3.3) is a recurring theme in target analysis.

2.7.6. Multi-pulse excitation models

Multi-pulse spectroscopy can provide extra information with which complicated compartmental schemes can be unravelled [7]. When a second pulse interacts with an excited state, three processes can occur: (i) when the state is emissive at the wavelength of the second exciting pulse, stimulated emission occurs, and the excited state returns to the ground state or to a ground state intermediate (GSI), which subsequently relaxes to the ground state. In this case, the second pulse is termed a dump pulse. (ii) When the state shows excited state absorption at the wavelength of the second exciting pulse, a higher excited state is created, which subsequently relaxes, possibly through the same or very similar intermediate states. (iii) When an excited state is already present, and a new excited state is created, singlet–singlet annihilation can occur. To isolate the effect of the second exciting pulse from a possible ground state excitation, the effect of the second pulse alone is subtracted from the measurement with both exciting pulses. Formally this can be described as follows:

$$\Delta A_{\mathrm{PP}}(t,\lambda) = \left(\sum_{l=1}^{n_{\mathrm{comp}}} c_{l,\mathrm{PP}}(t)\varepsilon_l(\lambda)\right) \oplus i_{\mathrm{PP}}(t) \qquad (45)$$

where the subscript PP indicates the ordinary pump-probe difference absorption experiment. Now the second pulse (which we call here the dump pulse) has an additional effect, which can be approximated by:

$$\Delta A_{\mathrm{PDP}}(t,\lambda) = \left(\sum_{l=1}^{n_{\mathrm{comp}}} c_{l,\mathrm{PDP}}(t)\varepsilon_l(\lambda)\right) \oplus i_{\mathrm{PDP}}(t-\Delta\mu) \qquad (46)$$

with $i_{\mathrm{PDP}}\ (t-\Delta\mu)$ being the IRF of the dump pulse administered after an interval $\Delta\mu$ with respect to the first, pump pulse. The interaction of the dump pulse with an Excited State Intermediate (ESI) results in the disappearance of part of the population of the ESI and possible appearance of GSI or another, higher ESI. Thus, the compartmental scheme of the $c_{l,PDP}\ (t)$ is in general extended with these new states. In the ideal case the dump pulse results in the enhanced population of a GSI, and introduces no new states. When this GSI decays faster than it is formed by normal decay of the ESI, the dump pulse uncovers the GSI. This is the case with the Green Fluorescent Protein [97,98]. After excitation of GFP, a proton is transferred resulting in a long-lived (ns) excited state, which is responsible for the green fluorescence. A second pulse resonant with this emission dumps this excited state resulting in a GSI. This GSI relaxes

in two steps of about 3 and 440 ps, whereby the proton is transferred back to the ground state. The pump-dump-probe technique in combination with the target analysis reveals the dynamics and the SADS of the states involved in this ground state proton transfer.

3. Parameter estimation

After formulation of a model for the observations (Eqs. (24), (25), (29), (32), (33) and (37)) the unknown parameters have to be estimated from the data. It is important to recognize that these equations represent a separable nonlinear model, also called partially linear model [24].

This means that, conditionally on the intrinsically nonlinear parameters θ, the conditionally linear parameters [25] (E in Eq. (24), C in Eq. (25), A in Eq. (30), a in Eq. (31), $\tilde{E}$ in Eq. (32), $\tilde{C}$ in Eq. (33), $\tilde{E}$ and fc in Eq. (37)) can be solved for using a special algorithm.

Because we assume additive normally distributed noise (Section 2.1.2) the nonlinear least squares estimator is also the maximum likelihood estimator, which in the ideal case results in maximal parameter precision [24,25]. The number of unknown parameters that need to be estimated can easily amount to several thousand, e.g. estimation of many spectra at hundreds of wavelengths with the help of a kinetic model (Eq. (24)). Therefore, it is crucial to reduce the dimensionality of the parameter search space by implicitly solving for the conditionally linear parameters. This is done by the Variable Projection algorithm developed in the seventies [85,99,100], which later became widely used in global analysis [19,101,102]. This algorithm exploits the bilinear structure of the model function. Crucial for precise parameter estimation is careful weighting of the observations [34]. After convergence of the nonlinear least squares fit routine, a further check of the neighbouring parameter space can be done using new starting values for the unknown parameters. This is elaborately discussed in Ref. [16]. Having estimated the parameters careful checking of the residuals is of paramount importance. With matrices of data, and thus also of residuals, the SVD is an ideal tool to check for structured residuals [92]. When the residuals are satisfactory, the parameter precision needs to be investigated. Linear approximation standard errors can be calculated from the Jacobian of the model function. With the Variable Projection algorithm the situation is somewhat more complicated. Here we present the equations for the kinetic model (Eq. (24)). Conditionally on the kinetic parameters θ, Eq. (24) represents a linear model. Therefore, the spectral parameters are estimated by:

$$\hat{E}^T(\theta) = C^{\dagger}(\theta)\Psi \tag{47}$$

where $C^{\dagger}(\theta)$ is the Moore–Penrose generalized inverse of $C(\theta)$, and the circumflex ^ denotes "estimator of". It can be proved that the approximate covariance matrix of the vector representation of $\hat{E}^T$ is given by (omitting the θ dependence for clarity):

$$\mathrm{cov}(\mathrm{vec}(\hat{E}^T)) = \hat{\sigma}^2(I_n \otimes C^{\dagger}C^{\dagger^T}) + G\mathrm{cov}(\hat{\theta})G^T \tag{48}$$

with $\hat{\sigma}^2$ the variance estimate, and with matrix G consisting of columns $\mathrm{vec}\left(C^{\dagger}\frac{\partial C}{\partial \theta_i}\hat{E}^T\right)$. In a simulation study [88], it was shown that the linear approximation standard error is adequate for the kinetic parameters, thus the model is functionally linear [103]. However, the linear approximation standard error is less adequate for the spectral parameters [104]. In that case likelihood-based confidence regions can be calculated [25,37,104].

3.1. Incorporating multiple experiments

A commonly occurring situation is when multiple experiments are done which are believed to be described by a single (most often kinetic) model, however, each experiment may possess some experiment-specific parameters. Examples are (i) measurement of time gated spectra in two or more different wavelength ranges, or under different polarization angles; (ii) trace measurements in different time ranges; (iii) measurements with varying instrument responses. In most of these cases global analysis is still applicable, but extra nuisance parameters may have to be introduced. E.g. because of laser power fluctuations, scaling parameters may be necessary to simultaneously analyse data from different experiments (case (ii)) [92]. This number of scaling parameters can become very large. The generalization of Eq. (37) to a simultaneous target analysis of multiple experiments is straightforward. For each extra experiment, an overall scaling parameter is needed, to account for variations in the product of sample OD and intensity of the actinic flash. With the five-way BR photocycle, this amounts to 235 scaling parameters, which is much more than the number of kinetic and spectral parameters [23].

3.2. Software

The modelling of time-resolved spectra is an iterative process, which benefits from a dedicated Problem Solving Environment [12,13,16,105] that incorporates a wide variety of models. The data analysis environment described in Refs. [12,13] concentrates on fluorescence data. The program described in Ref. [16] applies a simulated annealing strategy for estimation of the globally optimal model parameters. The implementation and application of the variable projection algorithm to global analysis was described in Ref. [101].

4. Case study: ultrafast dynamics of PYP

The purpose of this section is to apply the above presented methodology in a typical case study with real

three-way data sets. A chromophore–protein complex, the photoactive yellow protein (PYP) [5,6,91,92,106], was studied by time-resolved polarized difference absorption spectroscopy. The PYP chromophore (*p*-coumaric acid, pCA) is covalently bound to a 14-kDa protein, and then absorbs maximally at 446 nm (black spectrum in Fig. 9A). Upon excitation, PYP traverses a photocycle that eventually leads to a signaling state, most probably the pB state (also called I_2) mentioned in Section 2.7.4. The dynamics of the PYP photocycle extend from femtoseconds to seconds. In this experiment PYP was excited at 400 nm (blue pump spectrum in Fig. 9A). The early photophysics and photochemistry of this model system are discussed in detail elsewhere [8]. Here we present the modelling of three types of ultrafast data: we start with the magic angle (MA) data, then we add anisotropy data, and finally we test the kinetic scheme with multipulse data.

4.1. Residual analysis of MA data

The MA data (typical traces are shown in Fig. 3) were globally analysed using a parallel kinetic scheme (Section 2.4.1, Eq. (3)) with five lifetimes plus a coherent artefact. The uncorrected data (black) exhibit common noise, which is most clearly visible around 6, 100 and 400 ps. This is likely caused by baseline fluctuations in the data. To investigate this further, the matrix of residuals was subjected to Singular Value Decomposition (Eq. (23), Section 3). Fig. 4C shows that the first singular value is significantly larger than the remainder. The first right singular vector (w res, Fig. 4B) is almost flat in wavelength, whereas the first left singular vector (u res, Fig. 4A) displays no clear structure in time. These baseline fluctuations can be estimated from the residuals, and subtracted from the data, thus refining the analysis. The refined data are depicted in red in Fig. 3. This procedure results in a decrease of the root mean square error (rmse) from 0.85 to 0.42 mOD. Note that most of the fluctuations have been corrected for, as evidenced from the difference between the black and red solid lines. The results of SVD of the residual matrix from the refined global analysis have been depicted in Fig. 4D–F. Note that there appears to be no significantly larger first singular value in Fig. 4F. Judged from this residual analysis, and from the estimated parameters (vide infra), this global analysis is considered satisfactory.

4.2. Global analysis of MA data: DADS and EADS

The results from the global analysis of the MA data are shown in Fig. 5, using respectively a parallel (left) or a sequential (right) kinetic scheme. The concentrations of the components are depicted in Fig. 5A and B. When using a parallel scheme the estimated DADS are shown in Fig. 5C. Alternatively a sequential scheme with increasing lifetimes (Section 2.4.3.2) can be used resulting in Evolution Associated Difference Spectra (EADS), Fig. 5D. Note that both schemes result in exactly the same residuals and quality of fit of the data (Section 2.6.2). The DADS are interpreted as loss or gain of absorption with a certain lifetime, whereas the EADS represent the spectral evolution, e.g. the third EADS rises with the second lifetime and decays with the third lifetime. With simple systems the interpretation of the DADS or EADS can be straightforward. E.g. when the sequential scheme with increasing lifetimes represents the correct physicochemical picture, the EADS correspond to true Species Associated Difference Spectra (SADS) characterizing the intermediate states. In that case the DADS represent decay and rise of these states. With the complicated system here at hand the interpretation becomes an iterative process, and in fact the target analysis described below allows for a better interpretation of the DADS or EADS. At this point a number of comments are in order.

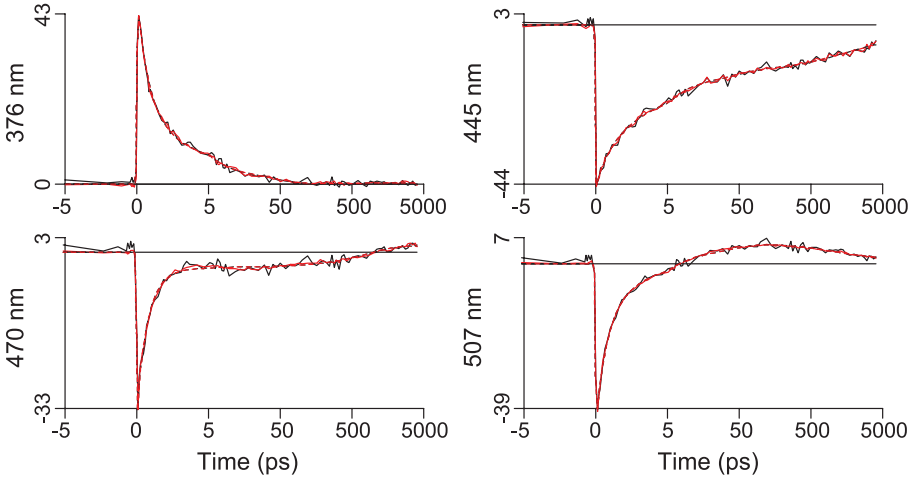

Fig. 3. Selected difference absorption traces (in mOD) of PYP after 400-nm excitation, measured at magic angle. Probe wavelength indicated along the ordinate. Uncorrected (black) and after correction for baseline fluctuations (red). Dashed lines indicate fit. Note that the time axis is linear from −5 to +5 ps relative to the maximum of the IRF, and logarithmic thereafter.

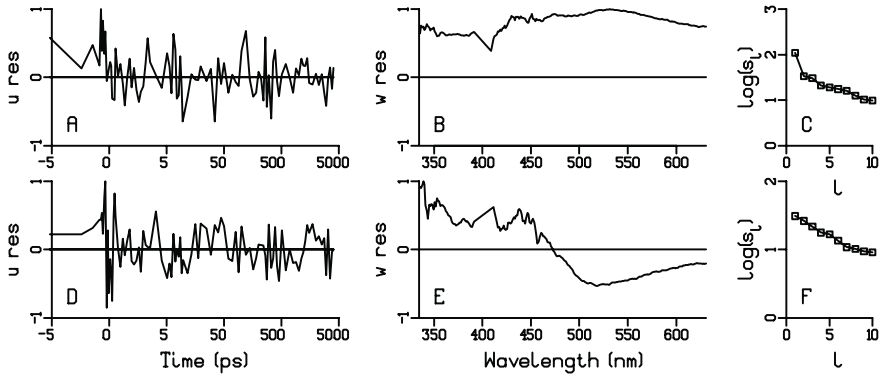

Fig. 4. Results from Singular Value Decomposition of the residual matrix. Top panels: uncorrected data. Bottom panels: residuals from data after correction for baseline fluctuations. (A, D) First left singular vector, showing dominant temporal structure. (B, E) First right singular vector, showing dominant spectral structure. (C, F) Singular values on logarithmic scale.

The first DADS (black) which decays in 0.8 ps shows a major loss of Excited State Absorption (ESA) from 340 to 420 nm and of Stimulated Emission (SE) from 460 to 630 nm. Less clear is a loss of Ground State Bleach (GSB, 420–460 nm). From the shape of the first DADS, it cannot be decided which states rise with 0.8 ps. The second DADS (red) decays in 3.3 ps. Again ESA loss is evident from 340 to 410 nm, as well as loss of SE (480–600 nm) and of GSB (410–460 nm). Note the large differences in shape between the first and second DADS which indicate the presence of other states. The third DADS (blue) decays in 34 ps. Its shape is similar to the second DADS (compare the normalized DADS in Fig. 5E). The fourth DADS (green, lifetime ≈ 1 ns) shows loss of GSB as well as loss of product state absorption (490–570 nm) which will later be ascribed to intermediate I_0. The fifth and final DADS (magenta) is long-

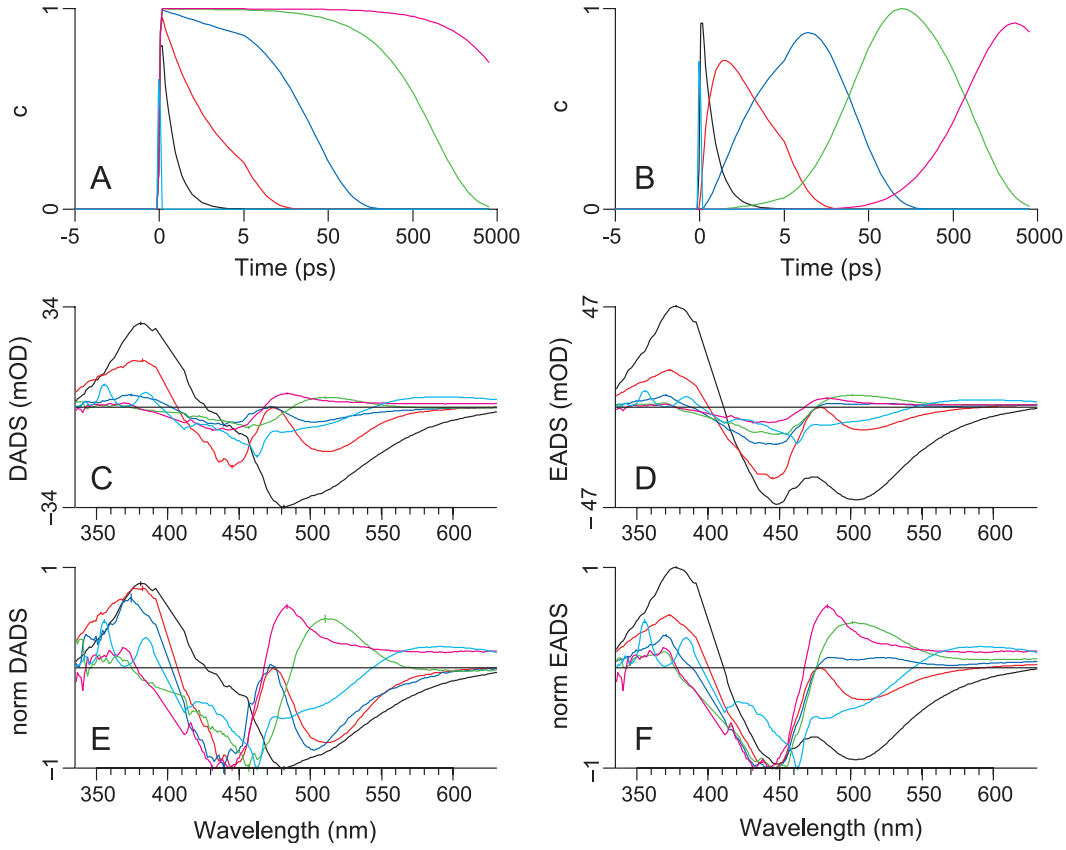

Fig. 5. Global analysis of PYP magic angle data using a parallel (left) or sequential kinetic scheme (right). (A, B) show $c(t)$ of the five components. Key: lifetime 0.8 ps (black), 3.3 ps (red), 34 ps (blue), 1 ns (green), long-lived (magenta). Coherent artefact with IRF time profile is in cyan. (C, D) depict estimated DADS and EADS. (E, F) show normalized spectra. Vertical bars indicate approximate standard errors.

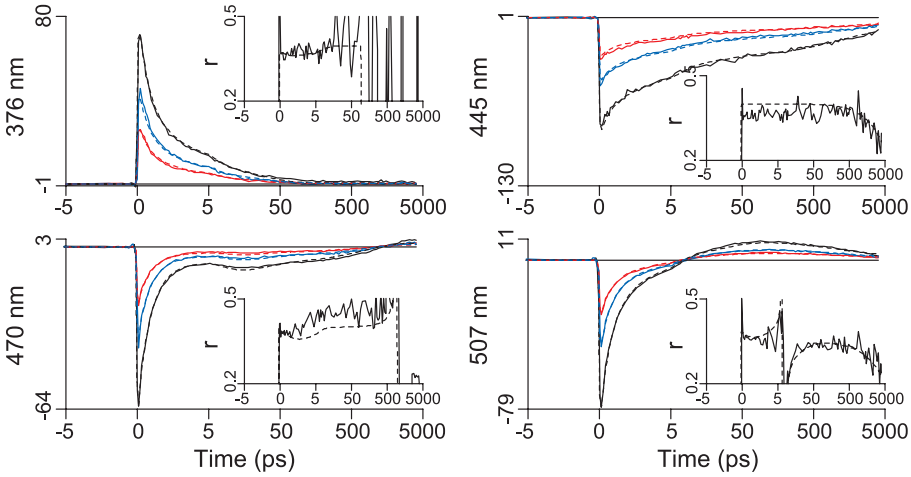

Fig. 6. Selected difference absorption traces (in mOD) of PYP after 400-nm excitation, measured at magic angle (blue), parallel (black), and perpendicular angle (red). Probe wavelength indicated along the ordinate. Insets depict raw anisotropy. Dashed lines indicate fit. Note that the time axis is linear from −5 to +5 ps relative to the maximum of the IRF, and logarithmic thereafter.

lived and represents the intermediate I_1. The coherent artefact is described by the cyan spectrum which is associated to the IRF. Depicted here is its contribution at the IRF maximum. This spectrum steals some amplitude from fast processes, e.g. early SE (470–540 nm) and solvated electron production (above 550 nm, explained below). Unless noted otherwise, the relative errors in the estimated lifetimes are about 10%. The estimated errors in the spectral parameters (see Eq. (48)) are also small, as evidenced by the error bars (vertical lines at extrema).

The first EADS (black in Fig. 5D) equals the sum of all DADS. Apart from the coherent artefact contribution, it represents the difference spectrum at time zero. It is characterized by a large GSB (420–460 nm). Note that the subsequent EADS show a gradual decrease of this GSB. The final EADS (magenta) equals the final DADS. If we assume that the evolution from the fourth to the fifth EADS corresponds to the transition from photocycle intermediates I_0 to I_1, then the fourth and fifth EADS represent the SADS of I_0 and I_1, respectively. The apparent loss of GSB in this transition could be due to non-unity quantum yield of this transition. Alternatively, the absorption of I_1 largely overlaps with the GSB, thus resulting in a smaller SADS. Both alternatives will be tested below. The second and third EADS are most difficult to interpret because at least three states contribute: excited state intermediates, I_0, and also a ground state intermediate (vide infra).

4.3. Target analysis of anisotropy data: SAS

To disentangle these complicated dynamics, more information is needed. Measurements at parallel and perpendicular polarization angles add information on anisotropy differences of the intermediates relative to the anisotropy of

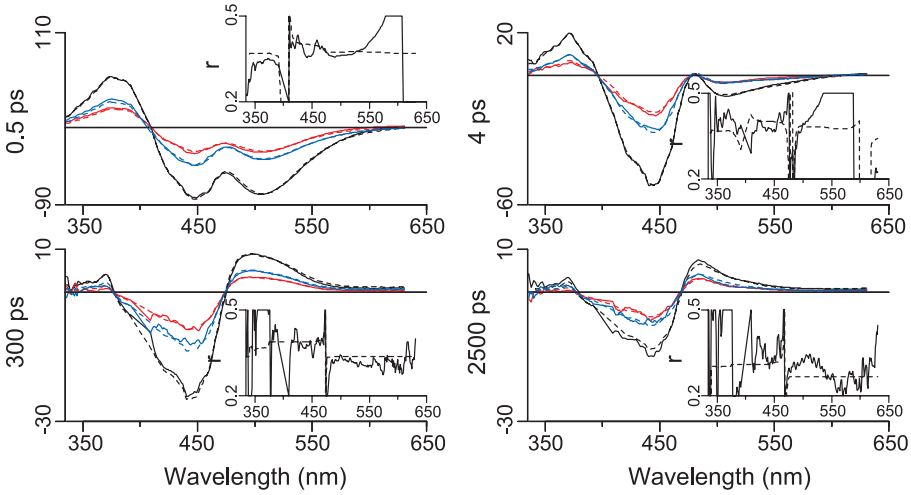

Fig. 7. Selected difference absorption spectra (in mOD) of PYP after 400-nm excitation, measured at magic angle (blue), parallel (black), and perpendicular angle (red). Probe time indicated along the ordinate. The two early spectra are affected by dispersion. Insets depict raw anisotropy. Dashed lines indicate fit.

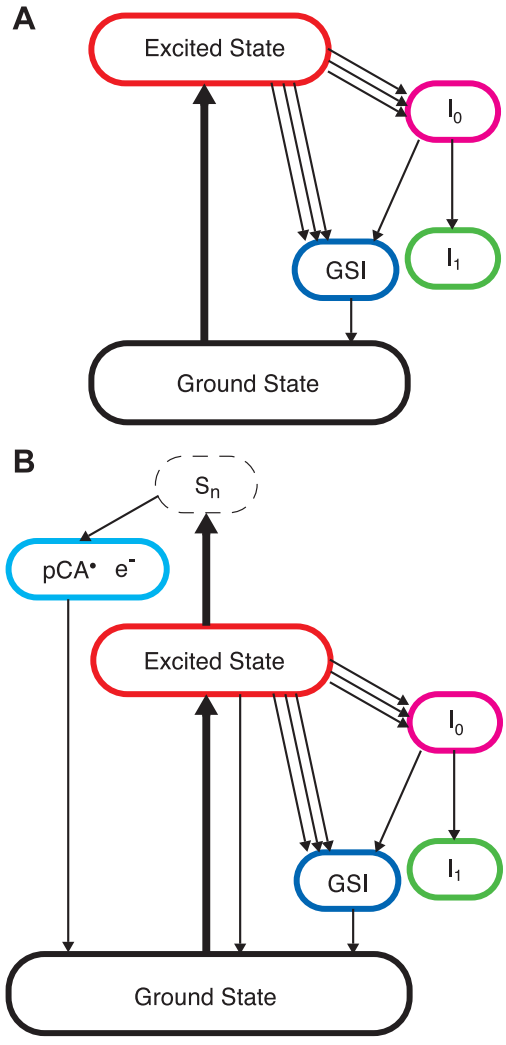

Fig. 8. Compartmental schemes for the target analysis of polarized transient difference absorption of PYP after 400 nm excitation. Vertical upward arrows indicate excitation. Excited state intermediates ESI1, 2 and 3 decay into I_0 or GSI. Scheme B differs from A by an additional decay from ESI1 to the ground state, and by a parallel photo ionization.

the GSB. Representative traces and spectra are shown in Figs. 6 and 7, respectively. Disregarding the dispersion, the 0.5-, 300- and 2500-ps spectra resemble the first, fourth and fifth EADS (Fig. 5F), respectively. The 4-ps spectrum resembles a mixture of the second and third EADS. For illustrative purposes only, the raw anisotropies $r(t,\lambda)$ (calculated according to Eq. (39)) are depicted in the insets of Figs. 6 and 7. Note that the $r(t, \lambda)$ are noisy, as explained in Section 2.7.5.1, and not suitable for further analysis.

A necessary prerequisite for the simultaneous analysis of the anisotropy data is a target model (Section 2.7.5.2). The target model consists of four parts: a compartmental scheme (Section 2.4.3) for the MA concentrations, a photocycle model (Section 2.7.4) which contains the SAS including the GSB (see Eq. (34)), an anisotropy model (Section 2.7.5.2) and spectral assumptions (Section 2.7.2) on the SAS. The compartmental scheme (Fig. 8A) consists of three Excited State Intermediates, ESI1, 2 and 3, each decaying monoexponentially (symbolized by the triple arrows), thus describing the three time scales of SE and ESA decay. This heterogeneity is not unusual for a biological system (Section 2.2.1). An alternative scheme with three interconverting states is discussed in Ref. [8]. An ESI can either decay into the photocycle intermediate I_0 or into the unrelaxed Ground State Intermediate (GSI). Subsequently, GSI relaxes to the ground state. As described above, the photocycle intermediate I_0 relaxes to the long-lived I_1. Of paramount importance for the fit of these anisotropy data with coexisting intermediates are the spectral assumptions which allow to describe parts of the data with a subset of the intermediates. The spectral assumptions used are: (i) GSB zero above 475

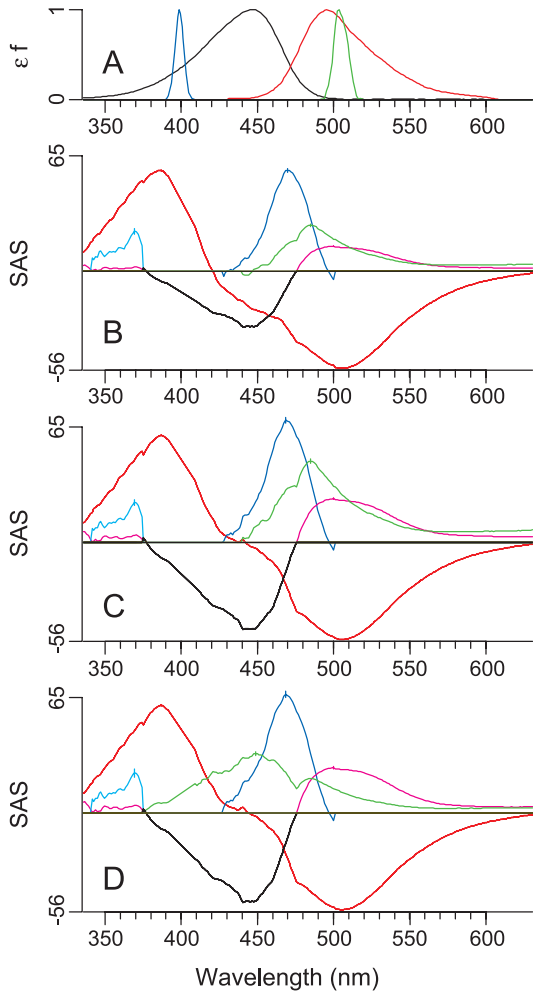

Fig. 9. (A) Normalized steady-state absorption (black) and emission (red) spectra of PYP, spectra of the pump pulse (blue) and of the dump pulse (green, applied in Fig. 10). (B, C, D) SAS estimated from the PYP anisotropy data using the compartmental schemes of Fig. 8. Panel B, corresponding to Fig. 8A, differs from panel C (which corresponds to Fig. 8B) by the absence of a decay from ESI1 to the ground state. Panel D differs from panel C in the SAS of I_1, it corresponds to Fig. 8B without the decay from I_0 to GSI. Key: GSB (black), ESI1, 2, 3 (red), GSI (blue), I_0 (magenta), I_1 (green), pCA radical (cyan). Coherent artefact has been omitted for clarity. Vertical bars indicate approximate standard errors.

nm, (ii) SAS of ESI1, 2 and 3 identical, (iii) SAS of GSI nonzero from 427 to 500 nm, (iv) SAS of I_0 zero below 475 nm, (v) SAS of I_1 zero below 440 nm. Although the anisotropy differences are small, they do allow resolution of the GSB spectrum (to which an anisotropy of 0.4 is assigned), and of the SAS of the intermediates (which possess somewhat lower anisotropies). The estimated SAS are shown in Fig. 9B. Instead of the five lifetimes from the global analysis, now seven lifetimes are estimated from the target analysis. Next to the long-lived GSB, an extra lifetime of 2.3 ps is estimated for the GSI. The SAS are all smooth, except for that of the ESI (red) which still appears to contain some bleach contribution from 420 to 460 nm. To improve the shape of the SAS of the ESI, an additional decay path from the ESI1 state directly to the ground state was added. Since this rate cannot be estimated from the fit, it was adjusted iteratively in order to produce a satisfactory shape. Actually a contribution of this path of 50% was used. Note that in Fig. 9C, the negative part of the ESI SAS (red) resembles the mirror image of the ground state SAS (black), analogous to the steady-state emission and absorption spectra in Fig. 9A. This shows that a rate parameter that does not influence the quality of fit of the data can be determined indirectly from the resulting SAS. In retrospect, we can now interpret the shape difference of the first and second DADS between 460 and 490 nm (Fig. 5E) and ascribe it to a rise of the GSI which accompanies the ESI1 decay.

Furthermore, a small long-lived product state absorption is present below 375 nm. This absorption was not influenced by the dump experiments (described in Section 4.4) and could therefore be attributed to resonantly enhanced photo ionization of the chromophore (*p*-coumaric acid, pCA) resulting in a radical and a solvated electron. It is possible to isolate this contribution from the GSB using spectral constraints. When the GSB is assumed to be zero below 375 nm, the long-lived signal

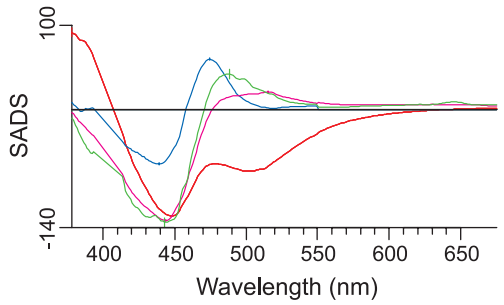

Fig. 11. SADS estimated from the PYP data with and without dump pulse (cf. Fig. 10) using the compartmental scheme of Fig. 8B. Key: SADS of ESI1, 2, 3 (red), GSI (blue), I_0 (magenta), I_1 (green). Coherent artefact has been omitted for clarity. Vertical bars indicate approximate standard errors.

below 375 nm can be attributed to the radical, resulting in the cyan SAS. The absorption of the solvated electron cannot be resolved, it is clearly visible in the long-lived DADS (magenta) above 570 nm in Fig. 5E. The anisotropies of ESI2, I_0 and I_1 were estimated to be, respectively, 0.33, 0.35 and 0.35, significantly lower than the 0.4 anisotropy of the GSB. The other anisotropies could not be precisely estimated.

As discussed in Section 4.2, an alternative interpretation of the loss of bleach in the transition from I_0 to I_1 is that the absorption of I_1 largely overlaps with the GSB. Thus, the spectral assumption (v), SAS of I_1 zero below 440 nm, can be replaced by a different assumption, namely that the quantum yield of the transition from I_0 to I_1 is unity, instead of 41% as estimated using the spectral assumption (v). This results in the I_1 SAS depicted in Fig. 9D. Although this modified kinetic scheme cannot be excluded, the spectral shape of the I_1 SAS is considered unlikely. This question can be resolved by a precise measurement of the wavelength dependence of the anisotropy at a few nanoseconds (before

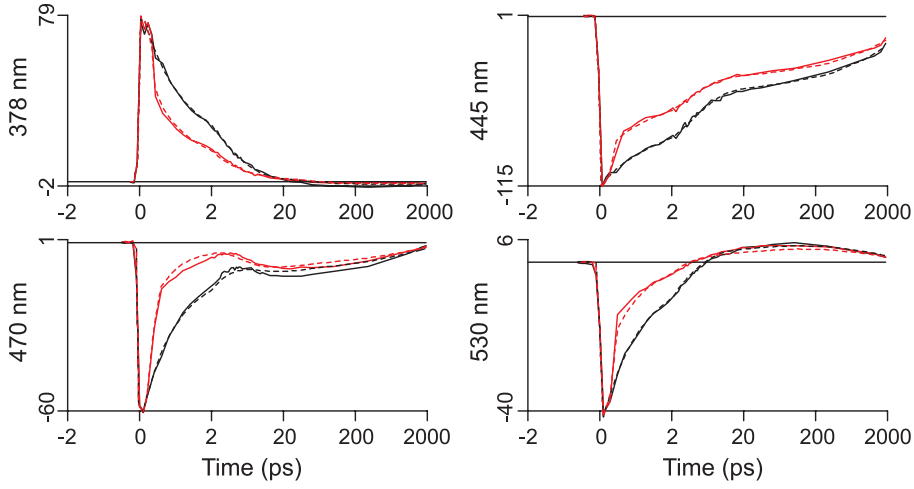

Fig. 10. Selected difference absorption traces (in mOD) of PYP after 400 nm excitation (black) and after a second dump pulse (red) centered around 505 nm (green in Fig. 9A) and administered ≈ 400 fs later. Probe wavelength indicated along the ordinate. Dashed lines indicate fit. Note that the time axis is linear from −2 to +2 ps relative to the maximum of the IRF, and logarithmic thereafter.

it disappears by tumbling, Eqs. (44), and 445 nm inset in Fig. 6), provided there is no photoionization present.

4.4. Target analysis of multipulse data: SADS

The compartmental scheme of Fig. 8B was put to the test with a multipulse experiment (Section 2.7.6). Administering a second laser pulse (green in Fig. 9A) resonant with the SE transfers population from excited to ground state intermediates. Thus, different concentrations of intermediates are created, providing new clues to resolve their properties. From the representative traces in Fig. 10 it becomes evident that the dump pulse depletes the ESI population resulting in decreased SE (530 nm), and decreased ESA (378 nm), concomitant with transient increased absorption at 470 nm. The last is attributable to the GSI. Also note the relatively small amount of GSB recovery (445 nm) upon application of the dump pulse, which also points to the presence of a GSI. Overall, the estimated SADS in Fig. 11 are consistent with the SAS of Fig. 9C. Unfortunately, the contribution of the radical and the solvated electron could not be resolved with these data, which were measured above 378 nm. The absorption by the solvated electron is clearly visible in the SADS of I_0 and I_1 above 570 nm. Both the anisotropy and the multipulse experiments are satisfactorily described by the kinetic scheme of Fig. 8B in combination with the anisotropy and IRF parameters, the SAS of Fig. 9C and the SADS of Fig. 11.

5. Conclusion

Global and target analysis are indispensable tools in the investigation of complex systems with time-resolved spectroscopy. In particular, multipulse experiments enable testing of complicated kinetic schemes. Spectrotemporal modeling offers a solution to the inverse problem, and allows precise estimation of the kinetic and spectral parameters that describe the complex system dynamics.

Acknowledgements

We thank Zsofia Derzsi, Marloes Groot, Klaas Hellingwerf, Dorte Madsen, Manolis Papagiannakis and Mikas Vengris for critically reading the manuscript and helpful discussions.

References

[1] A.R. Holzwarth, Time-resolved fluorescence spectroscopy, Methods Enzymol. 246 (1995) 334–362.
[2] H. van Amerongen, R. van Grondelle, Transient absorption spectroscopy in study of processes and dynamics in biology, Methods Enzymol. 246 (1995) 201–226.
[3] R.H. Lozier, R.A. Bogomolni, W. Stoeckenius, Bacteriorhodopsin: a light-driven proton pump in *Halobacterium halobium*, Biophys. J. 15 (1975) 955–962.
[4] T.G. Ebrey, Light energy transduction in bacteriorhodopsin, in: M.B. Jackson (Ed.), Thermodynamics of Membrane Receptors and Channels, CRC, Boca Raton, FL, 1993. Chap. 10.
[5] T.E. Meyer, E. Yakali, M.A. Cusanovich, G. Tollin, Properties of a water-soluble, yellow protein isolated from a halophilic phototrophic bacterium that has photochemical activity analogous to sensory rhodopsin, Biochemistry 26 (1987) 418–423.
[6] K.J. Hellingwerf, J. Hendriks, T. Gensch, Photoactive Yellow Protein, a new type of photoreceptor protein: will this "yellow lab" bring us where we want to go? J. Phys. Chem., A 107 (2003) 1082–1094.
[7] D.S. Larsen, M. Vengris, I.H.M. van Stokkum, M.A. van der Horst, F.L. de Weerd, K.J. Hellingwerf, R. van Grondelle, Photoisomerization and photoionization of the photoactive yellow protein chromophore in solution, Biophys. J. 86 (2004) 2538–2550.
[8] D.S. Larsen, I.H.M. van Stokkum, M. Vengris, M.A. van der Horst, F.L. de Weerd, K.J. Hellingwerf, R. van Grondelle, Incoherent manipulation of the photoactive yellow protein photocycle with dispersed pump-dump-probe spectroscopy, submitted for publication.
[9] R. Bro, J.J. Workman, P.R. Mobley, B.R. Kowalski, Review of chemometrics applied to spectroscopy: 1985–95: 3. Multi-way analysis, Appl. Spectrosc. Rev. 32 (1997) 237–261.
[10] S. Bijlsma, A.K. Smilde, Estimating reaction rate constants from a two-step reaction: a comparison between two-way and three-way methods, J. Chemom. 14 (2000) 541–560.
[11] J.M. Beechem, M. Ameloot, L. Brand, Global and target analysis of complex decay phenomena, Anal. Instrum. 14 (1985) 379–402.
[12] J.M. Beechem, A second generation global analysis program for the recovery of complex inhomogeneous fluorescence decay kinetics, Chem. Phys. Lipids 50 (1989) 237–251.
[13] J.M. Beechem, Global analysis program of biochemical and biophysical data, Methods Enzymol. 210 (1992) 37–54.
[14] M. Ameloot, N. Boens, R. Andriesen, V. van den Bergh, F.C. de Schryver, Compartmental analysis of fluorescence decay surfaces of excited state processes, Methods Enzymol. 210 (1992) 37–54.
[15] A.R. Holzwarth, Data analysis of time-resolved measurements, in: J. Amesz, A.J. Hoff (Eds.), Biophysical Techniques in Photosynthesis, Kluwer Academic Publishing, Dordrecht, the Netherlands, 1996, pp. 75–92.
[16] A.K. Dioumaev, Evaluation of intrinsic chemical kinetics and transient product spectra from time-resolved spectroscopic data, Biophys. Chem. 67 (1997) 1–25.
[17] R. Bonneau, J. Wirz, A.D. Zuberbühler, Methods for the analysis of transient absorbance data, Pure Appl. Chem. 69 (1997) 979–992.
[18] J.F. Nagle, L.A. Parodi, R.H. Lozier, Procedure for testing kinetic models of the photocycle of bacteriorhodopsin, Biophys. J. 38 (1982) 161–174.
[19] J.F. Nagle, Solving complex photocycle kinetics. Theory and direct method, Biophys. J. 59 (1991) 476–487.
[20] R.H. Lozier, A. Xie, J. Hofrichter, G.M. Clore, Reversible steps in the bacteriorhodopsin photocycle, Proc. Nat. Acad. Sci. U. S. A. 89 (1992) 3610–3614.
[21] R.W. Hendler, R.I. Shrager, S. Bose, Theory and procedures for finding a correct kinetic model for the bacteriorhodopsin photocycle, J. Phys. Chem., B. 105 (2001) 3319–3328.
[22] R.I. Shrager, R.W. Hendler, Critical evaluation of kinetic models for bacteriorhodopsin photocycles, J. Phys. Chem., B. 107 (2003) 1708–1713.
[23] I.H.M. van Stokkum, R.H. Lozier, Target analysis of the bacteriorhodopsin photocycle using a spectrotemporal model, J. Phys. Chem., B 106 (2002) 3477–3485.
[24] G.A.F. Seber, C.J. Wild, Nonlinear Regression, Wiley, New York, 1989.
[25] D.M. Bates, D.G. Watts, Nonlinear Regression and Its Applications, Wiley, New York, 1988.
[26] B. Gobets, The life and times of Photosystem I. Excitation energy transfer and trapping unravelled. Vrije Universiteit Amsterdam, 15 October 2002, PhD thesis.

[27] T. Ito, M. Hiramatsu, M. Hosoda, Y. Tsuchiya, Picosecond time-resolved absorption spectrometer using a streak camera, Rev. Sci. Instrum. 62 (1991) 1415–1419.
[28] M. van den Zegel, N. Boens, D. Daems, F.C. de Schryver, Possibilities and limitations of the time-correlated single photon counting technique: a comparative study of correction methods for the wavelength dependence of the instrument response function, Chem. Phys. 101 (1986) 311–335.
[29] N. Boens, N. Tamai, I. Yamazaki, T. Yamazaki, Picosecond single photon timing measurements with a proximity type microchannel plate photomultiplier and global analysis with reference convolution, Photochem. Photobiol. 52 (1990) 911–917.
[30] M. Zuker, A.G. Szabo, L. Bramall, D.T. Krajcarski, B. Selinger, Delta function convolution method (DFCM) for fluorescence decay experiments, Rev. Sci. Instrum. 56 (1985) 14–22.
[31] S.A. Kovalenko, A.L. Dobryakov, J. Ruthmann, N.P. Ernsting, Femtosecond spectroscopy of condensed phases with chirped supercontinuum probing, Phys. Rev., A 59 (1999) 2369–2384.
[32] I.H.M. van Stokkum, A.M. Brouwer, H.J. van Ramesdonk, T. Scherer, Multiresponse parameter estimation and compartmental analysis of time resolved fluorescence spectra. Application to conformational dynamics of charge-separated species in solution, Proc. K. Ned. Akad. v. Wet. 96 (1993) 43–68.
[33] S. Weisberg, Applied Linear Regression, 2nd ed., Wiley, New York, 1985.
[34] K.-H. Müller, T.H. Plesser, Variance reduction by simultaneous multi-exponential analysis of data sets from different experiments, Eur. Biophys. J. 19 (1991) 231–240.
[35] K.J. Laidler, Chemical Kinetics, 3rd ed., Harper and Row, New York, 1987.
[36] G.R. Fleming, T. Joo, M. Cho, Femtosecond chemical dynamics in condensed phases, Adv. Chem. Phys. 101 (1997) 141–183.
[37] T.A. Roelofs, C.H. Lee, A.R. Holzwarth, Global target analysis of picosecond chlorophyll fluorescence kinetics from pea chloroplasts. A new approach to the characterization of the primary processes in photosystem II α- and β-units, Biophys. J. 61 (1992) 1147–1163.
[38] S.W. Provencher, A constrained regularization method for inverting data represented by linear algebraic or integral equations, Comp. Phys. Commun. 27 (1982) 213–227.
[39] J.C. Brochon, Maximum-entropy method of data-analysis in time-resolved spectroscopy, Methods Enzymol. 240 (1994) 262–311.
[40] L.M.P. Beekman, I.H.M. van Stokkum, R. Monshouwer, A.J. Rijnders, P. McGlynn, R.W. Visschers, M.R. Jones, R. van Grondelle, Primary electron transfer in membrane-bound reaction centers with mutations at the M210 position, J. Phys. Chem. 100 (1996) 7256–7268.
[41] J.C. Hamilton, P.J. Gemperline, Mixture analysis using factor analysis: II. Self modeling curve resolution, J. Chemom. 4 (1990) 1–13.
[42] W. Windig, Self-modeling mixture analysis of spectral data with continuous concentration profiles, Chemom. Intell. Lab. Syst. 16 (1992) 1–16.
[43] L. Zimányi, A. Kulcsár, J.K. Lanyi, D.F. Sears, J. Saltiel, Singular value decomposition with self-modeling applied to determine bacteriorhodopsin intermediate spectra: analysis of simulated data, Proc. Natl. Acad. Sci. U. S. A. 96 (1999) 4408–4413.
[44] L. Zimányi, A. Kulcsár, J.K. Lanyi, D.F. Sears, J. Saltiel, Intermediate spectra and photocycle kinetics of the Asp96 → Asn mutant bacteriorhodopsin determined by singular value decomposition with self-modeling, Proc. Natl. Acad. Sci. U. S. A. 96 (1999) 4414–4419.
[45] A. Kulcsár, J. Saltiel, L. Zimányi, Dissecting the photocycle of the bacteriorhodopsin E204Q mutant from kinetic multichannel difference spectra. Extension of the method of singular value decomposition with self-modeling to five components, J. Am. Chem. Soc. 123 (2001) 3332–3340.
[46] S. Solar, W. Solar, N. Getoff, A pulse radiolysis-computer simulation method for resolving of complex kinetics and spectra, Radiat. Phys. Chem. 21 (1983) 129–138.
[47] K.J. Visscher, M.L. Hom, H. Loman, H.J.W. Spoelder, J.B. Verberne, Spectral and kinetic properties of intermediates induced by reaction of hydrated electrons with adenine, adenosine, adenylic acid and polyadenylic acid; a multi component analysis, Radiat. Phys. Chem. 32 (1988) 465–473.
[48] F.J. Knorr, J.M. Harris, Resolution of multicomponent fluorescence spectra by an emission wavelength-decay time data matrix, Anal. Chem. 53 (1981) 272–276.
[49] J.M. Beechem, M. Ameloot, L. Brand, Global analysis of fluorescence decay surfaces: excited-state reactions, Chem. Phys. Lett. 120 (1985) 466–472.
[50] J.R. Knutson, J.M. Beechem, L. Brand, Simultaneous analysis of multiple fluorescence decay curves: a global approach, Chem. Phys. Lett. 102 (1983) 501–507.
[51] J.E. Löfroth, Time-resolved emission spectra, decay-associated spectra, and species-associated spectra, J. Phys. Chem. 90 (1986) 1160–1168.
[52] V.N. Petushkov, I.H.M. van Stokkum, B. Gobets, F. van Mourik, J. Lee, R. van Grondelle, A.J.W.G. Visser, Ultrafast fluorescence relaxation spectroscopy of 6,7-dimethyl-(8-ribityl)-lumazine and riboflavin, free and bound to antenna proteins from bioluminescent bacteria, J. Phys. Chem., B 107 (2003) 10934–10939.
[53] R. Croce, M.G. Müller, R. Bassi, A.R. Holzwarth, Carotenoid-to-chlorophyll energy transfer in recombinant major light-harvesting complex (LHCII) of higher plants: I. Femtosecond transient absorption measurements, Biophys. J. 80 (2001) 901–915.
[54] M.G. Müller, J. Niklas, W. Lubitz, A.R. Holzwarth, Ultrafast transient absorption studies on Photosystem I reaction centers from *Chlamydomonas reinhardtii*: 1. A new interpretation of the energy trapping and early electron transfer steps in Photosystem I, Biophys. J. 85 (2003) 3899–3922.
[55] M. Bouchy, J.Y. Jezequel, J.C. Andre, J. Bordet, Problems arising from the quantization of the data in the mathematical treatment of single photon counting experiments, Deconvolution and Reconvolution of Analytical Signals. Application to Fluorescence Spectroscopy, E.N.S.I.C.-I.N.P.L., Nancy, France, (1982) 393–409.
[56] D.H. Anderson, Compartmental Modeling and Tracer Kinetics, Springer, Berlin, 1983.
[57] K. Godfrey, Compartmental Models and Their Application, Academic Press, London, 1983.
[58] A. Arcioni, C. Zannoni, Intensity deconvolution in fluorescence depolarization studies of liquids, liquid crystals and membranes, Chem. Phys. 88 (1984) 113–128.
[59] I.H.M. van Stokkum, L.M.P. Beekman, M.R. Jones, M.E. van Brederode, R. van Grondelle, Primary electron transfer kinetics in membrane-bound *Rhodobacter sphaeroides* reaction centers: a global and target analysis, Biochemistry 36 (1997) 11360–11368.
[60] S. Vajda, H. Rabitz, Identifiability and distinguishability of first-order reaction systems, J. Phys. Chem. 92 (1988) 701–707.
[61] J. Eisenfeld, C.C. Ford, A systems-theory approach to the analysis of multiexponential fluorescence decay, Biophys. J. 26 (1979) 73–84.
[62] I.H.M. van Stokkum, T. Scherer, A.M. Brouwer, J.W. Verhoeven, Conformational dynamics of flexibly and semirigidly bridged electron donor–acceptor systems as revealed by spectrotemporal parameterization of fluorescence, J. Phys. Chem. 98 (1994) 852–866.
[63] M.G. Müller, K. Griebenow, A.R. Holzwarth, Primary processes in isolated bacterial reaction centers from Rhodobacter sphaeroides studied by picosecond fluorescence kinetics, Chem. Phys. Lett. 199 (1992) 465–469.
[64] I. Chizhov, D.S. Chernavskii, M. Engelhard, K.-H. Mueller, B.V. Zubov, B. Hess, Spectrally silent transitions in the bacteriorhodopsin photocycle, Biophys. J. 71 (1996) 2329–2345.
[65] M.E. van Brederode, W.D. Hoff, I.H.M. van Stokkum, M.L. Groot, K.J. Hellingwerf, Protein folding thermodynamics applied to the photocycle of photoactive yellow protein, Biophys. J. 71 (1996) 365–380.

[66] I.H.M. van Stokkum, H. Linsdell, J.M. Hadden, P.I. Haris, D. Chapman, M. Bloemendal, Temperature-induced changes in protein structures studied by Fourier transform infrared spectroscopy and global analysis, Biochemistry 34 (1995) 10508–10518.
[67] R. Kubo, A stochastic theory of lineshape, Adv. Chem. Phys. 15 (1969) 101–127.
[68] R.A. Marcus, Relation between charge transfer absorption and fluorescence spectra and the inverted region, J. Phys. Chem. 93 (1989) 3078–3086.
[69] J.R. Lakowicz, Principles of Fluorescence Spectroscopy, Plenum, New York, 1983. Chap. 2.
[70] R.D.B. Fraser, E. Suzuki, Resolution of overlapping bands: functions for simulating band shapes, Anal. Chem. 41 (1969) 37–39.
[71] J.M. Sevilla, M. Dominguez, F. Garcia-Blanco, M. Blazquez, Resolution of absorption spectra, Comput. Chem. 13 (1989) 197–200.
[72] T. Pullerits, R. Monshouwer, F. van Mourik, R. van Grondelle, Temperature dependence of electron-vibronic spectra of photosynthetic systems. Computer simulations and comparison with experiment, Chem. Phys. 194 (1995) 395–407.
[73] G.H. Golub, C.F. van Loan, Matrix Computations, 2nd ed., Johns Hopkins Univ. Press, Baltimore, 1990. Chap. 8.
[74] R.I. Shrager, R.W. Hendler, Titration of individual components in a mixture with resolution of difference spectra, p*K*s, and redox transitions, Anal. Chem. 54 (1982) 1147–1152.
[75] R.I. Shrager, Chemical transitions measured by spectra and resolved using singular value decomposition, Chemom. Intell. Lab. Syst. 1 (1986) 59–70.
[76] E.R. Henry, J. Hofrichter, Singular value decomposition: application to analysis of experimental data, Methods Enzymol. 210 (1992) 129–192.
[77] R.W. Hendler, R.I. Shrager, Deconvolutions based on singular-value decomposition and the pseudoinverse—a guide for beginners, J. Biochem. Biophys. Methods 28 (1994) 1–33.
[78] E.R. Henry, The use of matrix methods in the modeling of spectroscopic data sets, Biophys. J. 72 (1997) 652–673.
[79] H. Satzger, W. Zinth, Visualization of transient absorption dynamics—towards a qualitative view of complex reaction kinetics, Chem. Phys. 295 (2003) 287–295.
[80] J.F. Nagle, Photocycle kinetics: analysis of Raman data from bacteriorhodopsin, Photochem. Photobiol. 54 (1991) 897–903.
[81] I. Szundi, J.W. Lewis, D.S. Kliger, Deriving reaction mechanisms from kinetic spectroscopy. Application to late rhodopsin intermediates, Biophys. J. 73 (1997) 688–702.
[82] D.S. Burdick, An introduction to tensor-products with applications to multiway data-analysis, Chemom. Intell. Lab. Syst. 28 (1995) 229–237.
[83] Y. Imamoto, M. Kataoka, F. Tokunaga, T. Asahi, H. Masuhara, Primary photoreaction of photoactive yellow protein studied by subpicosecond–nanosecond spectroscopy, Biochemistry 40 (2001) 6047–6052.
[84] M. Schmidt, S. Rajagopal, Z. Ren, K. Moffat, Application of singular value decomposition to the analysis of time-resolved macromolecular X-ray data, Biophys. J. 84 (2003) 2112–2129.
[85] G. Golub, V. Pereyra, Separable nonlinear least squares: the variable projection method and its applications, Inverse Probl. 19 (2003) R1–R26.
[86] M.L. Horng, J.A. Gardecki, A. Papazyan, M. Maroncelli, Subpicosecond measurements of polar solvation dynamics: coumarin 153 revisited, J. Phys. Chem. 99 (1995) 17311–17337.
[87] V.H. Vilchiz, J.A. Kloepfer, A.C. Germaine, V.A. Lenchenkov, S.E. Bradforth, Map for the relaxation dynamics of hot photoelectrons injected into liquid water via anion threshold photodetachment and above threshold solvent ionization, J. Phys. Chem., A 105 (2001) 1711–1723.
[88] I.H.M. van Stokkum, Parameter precision in global analysis of time resolved spectra, IEEE Trans. Instrum. Meas. 46 (1997) 764–768.
[89] A. Pandit, R.W. Visschers, I.H.M. van Stokkum, R. Kraayenhof, R. van Grondelle, Oligomerization of light-harvesting I antenna peptides of *Rhodospirillum rubrum*, Biochemistry 40 (2001) 12913–12924.
[90] O.F.A. Larsen, I.H.M. van Stokkum, M.L. Groot, J.T.M. Kennis, R. van Grondelle, H. van Amerongen, Different electronic states in 2-aminopurine revealed by ultrafast transient absorption and target analysis, Chem. Phys. Lett. 371 (2003) 157–163.
[91] J. Hendriks, I.H.M. van Stokkum, K.J. Hellingwerf, Deuterium isotope effects in the photocycle transitions of the photoactive yellow protein, Biophys. J. 84 (2003) 1180–1191.
[92] W.D. Hoff, I.H.M. van Stokkum, H.J. van Ramesdonk, M.E. van Brederode, A.M. Brouwer, J.C. Fitch, T.E. Meyer, R. van Grondelle, K.J. Hellingwerf, Measurement and global analysis of the absorbance changes in the photocycle of the photoactive yellow protein from *Ectothiorhodospira halophila*, Biophys. J. 67 (1994) 1691–1705.
[93] K. Ekvall, P. van der Meulen, C. Dhollande, L.-E. Berg, S. Pommeret, R. Naskrecki, J.-C. Mialocq, Cross phase modulation artifact in liquid phase transient absorption spectroscopy, J. Appl. Phys. 87 (2000) 2340–2352.
[94] B. Borucki, H. Otto, M.P. Heyn, Reorientation of the retinylidene chromophore in the K, L, and M intermediates of bacteriorhodopsin from time-resolved linear dichroism: resolving kinetically and spectrally overlapping intermediates of chromoproteins, J. Phys. Chem., B 103 (1999) 6371–6383.
[95] M.P. Heyn, B. Borucki, H. Otto, Chromophore reorientation during the photocycle of bacteriorhodopsin: experimental methods and functional significance, Biochim. Biophys. Acta 1460 (2000) 60–74.
[96] J.F. Nagle, L. Zimányi, J.K. Lanyi, Testing BR Photocycle kinetics, Biophys. J. 68 (1995) 1490–1499.
[97] M. Chattoraj, B.A. King, G.U. Bublitz, S.G. Boxer, Ultra-fast excited state dynamics in green fluorescent protein: Multiple states and proton transfer, Proc. Nat. Acad. Sci. U. S. A. 93 (1996) 8362–8367.
[98] J.T.M. Kennis, D.S. Larsen, I.H.M. van Stokkum, M. Vengris, J.J. van Thor, R. van Grondelle, Uncovering the hidden ground state of green fluorescent protein, submitted for publication.
[99] G.H. Golub, V. Pereyra, The differentiation of pseudo-inverses and nonlinear least squares problems whose variables separate, SIAM J. Numer. Anal. 10 (1973) 413–432.
[100] L. Kaufman, A variable projection method for solving separable nonlinear least squares problems, BIT 15 (1975) 49–57.
[101] G.H. Golub, R.J. LeVeque, Extensions and uses of the variable projection algorithm for solving nonlinear least squares problems, Proc. of the 1979 Army Numerical Analysis and Comp. Conf, ARO Report vol. 79-3, (1979) 1–12.
[102] S. Solar, W. Solar, N. Getoff, A semi-linear optimization model for resolving fast processes, J. Chem. Soc., Faraday Trans. 2, 79 1983, pp. 123–135.
[103] I. Brooks, D.G. Watts, K.K. Soneson, P. Hensley, Determining confidence intervals for parameters derived from analysis of equilibrium analytical ultracentrifugation data, Methods Enzymol. 240 (1994) 459–478.
[104] R. Pribić, I.H.M. van Stokkum, A. van den Bos, Inference regions of nonlinear parameters in global analysis, in: M. Blanke, T. Söderström (Eds.), Proceedings SYSID '94, 10th IFAC Symposium on System Identification, Danish Automation Society, Copenhagen, 1994, pp. 2.423–2.428.
[105] I.H.M. van Stokkum, H.E. Bal, A Problem Solving Environment for interactive modelling of multiway data, Concurrency Computat: Pract. Exper., accepted for publication.
[106] L. Ujj, S. Devanathan, T.E. Meyer, M.A. Cusanovich, G. Tollin, G.H. Atkinson, New photocycle intermediates in the photoactive yellow protein from Ectothiorhodospira halophila: picosecond transient absorption spectroscopy, Biophys. J. 75 (1998) 406–412.

Available online at www.sciencedirect.com

SCIENCE DIRECT®

Biochimica et Biophysica Acta 1658 (2004) 262

BIOCHIMICA ET BIOPHYSICA ACTA
BBA

www.bba-direct.com

Erratum

Erratum to "Global and target analysis of time-resolved spectra" [Biochimica et Biophysica Acta 1658/2–3 (2004) 82–104]

Ivo H.M. van Stokkum*, Delmar S. Larsen, Rienk van Grondelle

Department of Physics and Astronomy, Faculty of Sciences, Vrije Universiteit, De Boelelaan 1081, 1081 HV Amsterdam, The Netherlands

The publisher regrets that in the abovementioned article the following corrections were not well implemented.

Page 85, right column, line 31 from the top "product ε_l" should read "product $c_l\varepsilon_l$".

Page 85, right column, line 34 from the top "and" should read "for c_l and".

Page 86, right column, line 1 from the top "$(2\sqrt{2\log}(2))$" should read "$(2\sqrt{2\log}(2))$".

Page 90, left column, line 4 from the top "and $(\bar{v})$ is" should read "and $f(\bar{v})$ is".

Page 90, left column, line 14 from the top "$((d)/(d\bar{v}))\varepsilon(\bar{v})/d\bar{v}=0$" should read "$d\varepsilon(\bar{v})/d\bar{v}=0$".

Page 90, left column, line 30 from the top "$\varepsilon\bar{v}$" should read "$\varepsilon(\bar{v})$".

Page 90, right column, line 36 from the top "$m\times n$" should read "$m\times m$".

Reference 8 in this article has been published in Biophys. J. 87(2004)1858–1872.

DOI of original articles 10.1016/j.bbabio.2004.04.011.

* Corresponding author.
E-mail address: ivo@nat.vu.nl (I.H.M. van Stokkum).

doi:10.1016/j.bbabio.2004.08.005